PCLAF-DREAM Drives Alveolar Cell Plasticity for Lung Regeneration

Bongjun Kim,[1] Yuanjian Huang,[1] Kyung-Pil Ko,[1] Shengzhe Zhang,[1] Gengyi Zou,[1] Jie Zhang,[1] Moon Jong Kim,[1] Danielle Little,[2] Lisandra Vila Ellis,[2] Margherita Paschini,[3] Sohee Jun,[1] Kwon-Sik Park,[4] Jichao Chen,[2] Carla Kim,[3] Jae-Il Park[1,5,6,*]

[1]Department of Experimental Radiation Oncology, Division of Radiation Oncology, The University of Texas MD Anderson Cancer Center, Houston, TX 77030, USA
[2]Department of Pulmonary Medicine, The University of Texas MD Anderson Cancer Center, Houston, TX 77030, USA
[3]Stem Cell Program and Divisions of Hematology/Oncology and Pulmonary Medicine, Boston Children's Hospital, Boston, MA 02115, USA
[4]Department of Microbiology, Immunology, and Cancer Biology, University of Virginia, Charlottesville, VA 22908, USA
[5]Graduate School of Biomedical Sciences, The University of Texas MD Anderson Cancer Center, Houston, TX 77030, USA
[6]Program in Genetics and Epigenetics, The University of Texas MD Anderson Cancer Center, Houston, TX 77030, USA

*Correspondence: Jae-Il Park
E-mail: jaeil@mdanderson.org; Tel: 713-792-3659; Fax: 713-794-5369
Keywords: PCLAF, PAF, KIAA0101, DREAM complex, cell plasticity, lung regeneration, alveolar cells, phenelzine

One Sentence Summary

PCLAF-DREAM-driven cell plasticity is essential for lung regeneration, pharmacologically manipulated as a preventive strategy for lung fibrosis.

Abstract

The spatiotemporal orchestration of stem/progenitor cells is essential for lung regeneration, the failure of which leads to lung disease, including fibrosis. However, the mechanism of alveolar cell plasticity during regeneration remains elusive. We previously found that PCLAF remodels the DREAM complex for cell quiescence exit and cell proliferation. PCLAF is expressed explicitly in pulmonary proliferative cells, along with the DREAM target genes. Pclaf expression and Pclaf-expressing cells were acutely increased upon lung injury. Intriguingly, *Pclaf* knock-out mice exhibited lung fibrosis resulting from alveolar type I (AT1) cell loss. The single-cell transcriptome and organoid analyses showed that Pclaf-DREAM complex–transactivated gene expression is required for alveolar type II (AT2) cell transition into AT1. Mechanistically, Clic4, transactivated by the Pclaf-DREAM complex, activates TGF-β signaling for AT2-PPCs-AT1 cell lineage trajectory. Furthermore, pharmacological mimicking of the Pclaf-mediated transcriptome markedly increased alveolar regeneration. Our study unveils an unexpected role of the PCLAF-DREAM axis in controlling alveolar cell plasticity for lung regeneration and proposes a viable option for lung fibrosis prevention.

Introduction

Lung disease is one of the leading causes of death, with one in six deaths worldwide (*1*). Various environmental pathogens and stresses cause lung injuries (*2-4*). Stem and progenitor cell–driven regenerative potency functionally restores damaged lungs (*5, 6*). The failure of lung stem/progenitor cell activation or differentiation results in lung disease, including pulmonary fibrosis (*5-8*). Alveolar type II (AT2) cells have been suggested as a pivotal cell type in lung regeneration. Dysregulation of the facultative progenitor capacity of AT2 cells induces lung fibrosis rather than regeneration (*7, 9-13*). Downregulation of Toll-like receptor 4-hyaluronan interaction (*7*) and sustained mechanical tension (*13*) inhibits AT2 cell stemness and plasticity. Telomere dysfunction (*10*) and mutant surfactant protein C (SPC) (*11*) promote AT2 cell hyperplasia, causing the failure of lung regeneration. Therefore, the precise control of AT2 cells is vital for lung regeneration. However, the detailed mechanism of AT2 cell activation and plasticity remains ambiguous.

The dimerization partner, retinoblastoma (RB)-like, E2F, and multi-vulval class B (DREAM) complex is an evolutionarily conserved multiprotein complex that orchestrates cell quiescence and the cell cycle (*14-17*). Dissociation of the multi-vulval class B (MuvB) core complex with RBL2 (retinoblastoma-like protein 2/p130), E2F4, and DP1 (E2F dimerization partner 1) drives the MuvB complex to bind to BYMB and FOXM1, transactivating cell cycle-related DREAM target genes and leading to cell quiescence exit and cell proliferation (*18*). We recently found that proliferating cell nuclear antigen–associated factor (PCLAF/PAF/KIAA0101) remodels the DREAM complex to bypass cell quiescence and promote cell proliferation (*19*). PCLAF is also indispensable for cell stemness and the plasticity of breast cancer cells and intestinal stem cells (*20, 21*). These studies led us to evaluate the role of PCLAF in lung regeneration.

Results

PCLAF-positive cells are elevated during lung regeneration

We first characterized PCLAF-positive cells in the lungs by analyzing the data set of single-cell RNA-sequencing (scRNA-seq) of murine (GSE141259) and human (GSE135893) lung tissues. The mouse lungs showed that Mki67$^+$ pulmonary proliferating cells (PPCs) specifically expressed *Pclaf* (Fig. 1, A to C). These PPCs barely expressed mature lung epithelial cell markers or lung stem/progenitor cell markers (Fig. S1, A, C, and D, and Data file S1). The human lungs also showed specific expression of PCLAF in PPCs (Fig. 1, D to F, Fig. S1, B, E, and F, and Data file S2). To understand the role of PCLAF in lung regeneration, we utilized a bleomycin-induced lung injury mouse model, widely used to study lung injury, regeneration, and fibrosis (*22*). Upon the instillation of bleomycin, the number of PPCs was elevated in the mouse lungs (Fig. 1G). Bleomycin injury also led to increased *Pclaf* expression, which peaked at 7 days post-injury (dpi) and decreased at 14 dpi in the mouse lung tissues (Fig. 1H), consistent with the immunostaining results for Pclaf (Fig. 1I). In addition, *Pclaf-lacZ* knock-in mice displayed a similar increase in Pclaf$^+$ cells in the regenerating lungs (Fig. 1, J to L).

Pclaf is indispensable for repopulation of AT1 cells during lung regeneration

Next, to determine the role of PCLAF in lung regeneration, we administered a low dose of bleomycin (1.4 U/kg) to *Pclaf* wild-type (WT) and knock-out (KO) mice (Fig. 2A). Bleomycin initially damages the alveolar epithelium, including alveolar type I (AT1) and AT2 cells, followed by inflammation and interstitial fibrosis (*22-24*). At the early stage of bleomycin administration, both *Pclaf* WT and KO mice exhibited a gradual decrease in blood oxygen levels (peripheral oxygen saturation [SpO_2]) and breath rate per minute until 5 dpi (Fig. 2B). Interestingly, *Pclaf* KO mice showed the attenuated and delayed restoration of SpO_2 saturation and breath rate per minute at 9 dpi and decreased O_2 saturation at 21 dpi (Fig. 2B). At the acutely damaged stage (3 dpi), both *Pclaf* WT and KO mice showed a severely reduced number of $Rage^+$ (AT1) and Spc^+ (AT2) cells (Fig. 2, C and D, and Fig. S2). However, consistent with the results of pulmonary functional analysis, *Pclaf* KO showed decreased AT1 cells at the regeneration stage (7 dpi) and chronic fibrosis stage (21 dpi) (Fig. 2, C and D, and Fig. S2). Intriguingly, the number of AT2 cells was elevated in *Pclaf* KO mice upon bleomycin (Fig. 2, C and D, and Fig. S2). Unlike WT lung tissues, *Pclaf* KO lungs exhibited more inflamed and condensed tissue (Fig. 2E), with severe fibrotic features confirmed by picrosirius red (a dye staining collagen) and αSma/Acta2 (a marker for myofibroblasts) staining (Fig. 2, F to H). These results suggest that Pclaf is indispensable for bleomycin-induced lung regeneration.

AT2 cells replenish AT1 cells during lung regeneration (*25*). Having observed that *Pclaf* KO impaired lung regeneration with the aberrantly increased AT2 cells, we next determined the impact of *Pclaf* KO on cell plasticity between AT2 and AT1 cells by using lung organoids (LOs). We evaluated the lung organoid-forming efficiency (OFE) and cellular heterogeneity generation of two different LO culture methods, co-culture systems with lung endothelial cells (LuECs) or lung mesenchymal cells (LuMSCs) in the 3D organoid air-liquid interface (Fig. S3A) (*26-28*). Both culture methods were sufficient to grow LOs (Fig. S3A). While LOs with LuMSCs were mainly differentiated into the bronchiolar type, LOs co-cultured with LuECs developed into both alveolar and bronchiolar types of LOs (Fig. S3, B to D), which led us to choose LuECs as stromal cells for subsequent LO experiments. We isolated and cultured lung epithelial cells ($Epcam^+/Ter119^-/Cd31^-/Cd45^-$) from *Pclaf* WT or KO mice at 7 dpi (bleomycin) with LuECs (Fig. 2I). Notably, OFE was reduced in *Pclaf* KO cells compared to in *Pclaf* WT cells (Fig. S4, A and B). In addition, *Pclaf* KO LOs showed fewer alveolar (~12%) and bronchioalveolar types (~50%), whereas *Pclaf* WT LOs displayed alveolar (~27%) and bronchioalveolar types (~70%) (Fig. S4, C and D). Interestingly, the bronchiolar type of LOs was generated only by *Pclaf* KO (~29%) (Fig. S4, C and D). Moreover, *Pclaf* KO alveolar-type LOs showed fewer AT1 cells, consistent with in vivo results (Fig. 2, J and K). These data indicate that Pclaf is required for the plasticity of AT1 and AT2 cell lineage during lung regeneration.

Pclaf KO suppresses AT2 cell lineage plasticity

To further explore the cellular mechanism of Pclaf-controlled lung regeneration, we leveraged single-cell transcriptomics. We isolated pulmonary epithelial cells from *Pclaf* WT or KO lung tissues at 7 dpi (bleomycin) and performed scRNA-seq (Fig. S5A). Cells were clustered and annotated based on the established cell markers (Fig. 3, A and B, Fig. S5B, Fig. S6, and Data file S3). The AT2 cells were refined into two subsets, AT2 ($Lcn2^{high}$) and AT2 ($Slc34a2^{high}$) cells (Fig.

3B, Fig. S6, D and E). Consistent with the in vitro and in vivo results, *Pclaf* KO lungs showed reduced AT1 cells and elevated AT2 (Slc34a2^{high}) cells (Fig. 3, B and C). Additionally, AT2^{med}/AT1^{med} cells, transitioning cells from AT2 into AT1 (*29, 30*), were decreased in *Pclaf* KO mice (Fig. 3, B and C). In line with previous studies (*25, 29, 30*), an RNA velocity–based cell lineage trajectory analysis showed the cellular trajectory from AT2 cells into AT1 cells in *Pclaf* WT (Fig. 3, D to F, and 3H). AT2 (Lcn2^{high}) cells serve as root cells that differentiate into AT1 cells through two different paths, via AT1^{med}/AT2^{med} cells or PPCs and Krt8^{+} cells. Additional cell lineage trajectories from AT2 (Lcn2^{high}) cells to AT2 (Slc34a2^{high}) cells through PPCs were observed (Fig. 3, D to F, and 3H). Unlike *Pclaf* WT, *Pclaf* KO lung showed a favored trajectory of PPCs into AT2 (Slc34a2^{high}) cells (Fig. 3, D to F, and 3H). Additionally, in *Pclaf* KO lungs, Krt8^{+} cells and AT1^{med}/AT2^{med} cells showed lineage trajectories into AT2 (Lcn2^{high}) and AT2 (Slc34a2^{high}) cells, respectively, rather than toward AT1 cells (Fig. 3, D to F, and 3H). Consistently, the CytoTRACE analysis showed a less differentiated cell status in transitioning AT1^{med}/AT2^{med} cells of *Pclaf* KO lungs than of WT lungs (Fig. 3G). While AT2 cells self-renewed and differentiated into AT1 cells via PPCs for normal lung regeneration, *Pclaf* KO impaired AT1 differentiation from PPCs derived from AT2 cells (Fig. 3H). These results suggest that Pclaf promotes the cell plasticity of AT2 and PPCs into AT1 for lung regeneration.

PCLAF-DREAM axis is required for AT1 cell differentiation cells during lung regeneration

Next, we sought to elucidate the underlying mechanism of PCLAF-controlled AT2 cell plasticity. PCLAF remodels the repressive DREAM complex to activate the target gene transcription (*19*). Consistent with the specific expression of PCLAF/Pclaf in PPCs, the expression of DREAM target genes was exclusively enriched in the PPCs of human and mouse lung tissues (Fig. 4, A and B, and Fig. S7A), also confirmed by gene set enrichment analysis (GSEA) of *Pclaf* WT vs. KO lung tissues (Fig. 4C, and Fig. S7B). Intriguingly, *Pclaf* KO PPCs displayed lower expression of the DREAM target genes than did *Pclaf* WT PPCs (Fig. 4D), implying that the DREAM complex might be functionally associated with PCLAF-controlled AT2 cell plasticity. To test this, we pharmacologically and genetically manipulated the DREAM complex in the LOs isolated from the mice treated with bleomycin. First, we used harmine, an inhibitor of DYRK1A that suppresses the DREAM complex (*31, 32*). DYRK1A-phosphorylated serine residue (Ser28) of LIN52, a core subunit of the DREAM/MuvB complex, is essential for recruiting RBL2/p130, E2F4, and DP1 to the MuvB core complex to form a repressive DREAM complex, which subsequently suppresses gene transactivation. Thus, harmine-inhibited DYRK1A constitutively activates DREAM target gene expression. Harmine treatment rescued OFE inhibited by *Pclaf* KO (Fig. 4, E to G). Harmine also restored the lung regeneration impaired by *Pclaf* KO, with increased AT1 and decreased AT2 cells (Fig. 4, H and I). Moreover, the ectopic expression of the Lin52-S28A mutant, which is no longer phosphorylated by DYRK2 and consequently activates the DREAM target gene expression, rescued the *Pclaf* KO phenotype by AT1 cell repopulation, restored the number of AT2 cells, and increased OFE (Fig. 4, J to L, and Fig. S8). WNT signaling maintains AT2 cell stemness (*33*). Although PCLAF hyperactivates WNT/β-catenin in the intestine (*21, 34*), β-catenin target genes (*Cd44*, *Ccnd1*, and *Bmp4*) were marginally downregulated in *Pclaf* KO PPCs. Additionally, the Sox9-based progenitor gene signature, which positively regulates lung stem/progenitor cell plasticity (*35*), and *Myc* transactivated by Pclaf in the intestine (*21*) were not downregulated in

165 *Pclaf* KO PPCs (Fig. S9). These results suggest that the PCLAF-DREAM axis–controlled
166 transcriptome mediates alveolar cell lineage plasticity for lung regeneration.

167 PCLAF-DREAM-activated CLIC4-TGFβ signaling axis is required for AT1 cell 168 differentiation

169 Among the differentially expressed genes (DEGs; *Pclaf* WT vs. KO) of the DREAM target genes,
170 *Clic4* showed reduced expression in transitioning cells (PPC, Krt8^{+}, and AT2^{med}/AT1^{med} cells (Fig.
171 S10A), validated by immunostaining (Fig. 5, A and B). CLIC4 is an integral component of TGF-
172 β signaling, required to transdifferentiate AT2 cells into AT1 cells during lung regeneration (*36,*
173 *37*). CLIC4 positively modulates TGF-β signaling by preventing the dephosphorylation of
174 phospho-SMAD2/3 in the nucleus (*38, 39*). Given the crucial role of TGF-β/SMAD signaling in
175 the lung regeneration (*36, 37*), we hypothesized that the PCLAF-DREAM-activated CLIC4-TGF-
176 β signaling axis is required for AT2 cell plasticity into AT1 cells. Indeed, SMAD3 target genes
177 from three datasets (*40, 41*) were downregulated in *Pclaf* KO PPCs but not in other cell types
178 compared to WT (Fig. 5C). In addition, a GSEA showed the enrichment of Smad2 or Smad3 target
179 gene expression in *Pclaf* WT PPCs compared to in *Pclaf* KO PPCs (Fig. 5D, and Fig. S7B).
180 Moreover, a SCENIC gene network analysis showed reduced Smad3 regulon activity in *Pclaf* KO
181 PPCs and Krt8^{+} cells (Fig. 5E), consistent with the reduced p-Smad3 in the lung of *Pclaf* KO mice
182 treated with bleomycin, compared to the *Pclaf* WT regenerating lung (Fig. 5, F and G). Conversely,
183 harmine treatment restored Clic4 and p-Smad3 expression downregulated by *Pclaf* KO (Fig. S10,
184 B to E). Next, to determine the role of the CLIC4-TGF-β signaling axis in AT2 cell plasticity, we
185 ectopically expressed Clic4 in *Pclaf* KO LOs. Clic4 expression increased phosphorylation of
186 Smad3 (Fig. S10, F and G) and rescued the AT1 differentiation blocked by *Pclaf* KO (Fig. 5, H to
187 J, and Fig. S10H), as did temporarily controlled TGF-β treatment (Fig. 5, K to N, and Fig. S11).
188 Notably, human PPCs from idiopathic pulmonary fibrosis (IPF) showed reduced CLIC4 and
189 SMAD3-target genes expression compared to PPCs from normal lungs (Fig. 5, O and P). TGF-β
190 signaling also contributes to lung fibrosis (*42*). While regenerating alveoli lesions showed
191 decreased p-Smad3 by *Pclaf* KO, the inflamed lesions exhibited elevated p-Smad3 (Fig. S12).
192 Additionally, human IPF fibroblasts showed increased SMAD3-target gene expression compared
193 to normal lung fibroblasts (Fig. S13). These results suggest that the PCLAF-DREAM-activated
194 CLIC4-TGF-β axis is required for AT2 cell plasticity in lung regeneration.

195 Pharmacological mimicking of PCLAF-DREAM-activated transcriptional signature 196 attenuates lung fibrosis

197 For the pharmaceutical application of PCLAF-DREAM-controlled lung regeneration, we
198 exploited the perturbational datasets (L1000) using the CLUE platform (*43*), identifying drug
199 candidates that mimic PCLAF-activated transcriptional signatures. Since PCLAF also promotes
200 lung tumorigenesis (*19*), to minimize the risk of tumorigenesis by drug candidates, we excluded
201 any drugs that were identified from the Pclaf/PCLAF depleted gene sets of the mouse lung tumors
202 (*Kras^{G12D}/Trp53$^{-/-}$*; KP) and human (H1792) lung cancer cell lines (Fig. 6, A and B, and Data file
203 S4 and S5) (*19*), which identified four drugs (phenelzine, trimethobenzamide, ibuprofen, and RS
204 23597-190) (Fig. 6B). Among those, phenelzine, an FDA-approved anti-depressor, increased OFE
205 (Fig. S14) and AT1 cells in LOs (Fig. 6, C and D). Additionally, phenelzine reduced the numbers

206 of ciliated cells and elevated club cells in LOs (Fig. 6, C and D). Next, we tested the impact of
207 phenelzine on lung regeneration in mice given a high dosage of bleomycin (2.7 U/kg). Phenelzine
208 ameliorated bleomycin-decreased SpO_2 levels (Fig. 6F) and markedly reduced lung fibrosis with
209 a restored AT1 cell repopulation (Fig. 6, G to J). These data suggest that phenelzine, a PCLAF
210 activation–mimicking drug, has therapeutic efficacy in lung regeneration and fibrosis.

211 **Discussion**

212 Accumulating evidence suggests that during alveolar regeneration, AT2 cells act as progenitor
213 cells that differentiate toward AT1 cells through intermediate cell states. Such transient cells
214 express low levels of AT1 and AT2 markers and their specific genes, such as *Krt8 (25, 29, 30)*.
215 Several developmental signaling pathways (BMP (*44*), NOTCH (*44*), and YAP/TAZ (*45*))
216 contribute to cell transition from AT2 to AT1 during regeneration. However, the detailed
217 mechanism of AT2 cell lineage plasticity during regeneration remains elusive. Our study identified
218 a new role of the PCLAF-DREAM axis in cell plasticity (from AT2 to AT1). The primary function
219 of the DREAM complex in orchestrating the cell cycle and cell quiescence by transactivating or
220 repressing gene expression has mainly been investigated using in vitro systems (*17, 18, 46-51*).
221 Recently, we found that the deregulated DREAM complex promotes lung tumorigenesis in vivo
222 (*19*). Genome-wide analyses showed that most DREAM target genes are cell cycle-related genes
223 (*46, 50*) and genes involved in other biological processes (Data file S6). Given that the DREAM
224 complex coordinates the cell cycle (*17, 18, 46-50*), we initially hypothesized that the PCLAF-
225 DREAM axis induces mitotic activation of lung progenitor cells for regeneration. Indeed, the
226 expression of cell cycle-related genes (*Top2a* and *Mki67*) were decreased in *Pclaf* KO PPCs (Fig.
227 S10A) with reduced OFE (Fig. S4, A and B). However, *Pclaf* KO mice showed a slightly higher
228 number of PPCs than *Pclaf* WT mice (Fig. 3C), which might be due to "stalled" transitioning from
229 PPCs to $Krt8^+$ cells. Unlike *Pclaf* WT PPCs, which show cellular trajectory into AT2 ($Slc34a^{high}$)
230 and $Krt8^+$ cells during normal regeneration, *Pclaf* KO PPCs failed to differentiate into $Krt8^+$ cells
231 (Fig. 3, D to F, and 3H), which might result in an increased number of PPCs in *Pclaf* KO mice. In
232 addition, it should be noted that the number of AT2 ($Slc34a^{high}$) cells differentiated from PPCs was
233 elevated by *Pclaf* KO (Fig. 2 and 3). Intriguingly, our data also showed that DREAM complex–
234 mediated gene transactivation is indispensable for the differentiation of PPCs into AT1 cell lineage
235 (Fig. 4). Clic4 transactivated by the PCLAF-DREAM complex positively modulates TGF-β
236 signaling (*38*), driving PPCs to AT1 differentiation (Fig. 5). Our results unveil an unexpected role
237 of the DREAM complex in positively regulating cell plasticity and promoting tissue regeneration
238 beyond its canonical role in controlling cell quiescence and proliferation.

239 Despite the recent single-cell transcriptomics of the lungs (*29, 30, 35, 52*), the proliferating
240 cell clusters have not been studied. Herein, our results suggest that PPCs are the transitioning cells
241 during alveolar regeneration. Recently, Murthy et al. proposed that AT0 cells expressing *SFTPC*
242 and *SCGB3A2* transiently differentiate into AT1 cells in human lungs (*53*). These AT0 cells are
243 proliferating cells expressing MKI67 (*53*), consistent with our finding that PPCs are intermediate
244 transitioning cells generating AT1 cells.

245 TGF-β signaling has been proposed as one of the driving factors for lung fibrosis (*54*) by
246 promoting the epithelial-mesenchymal transition of AT2 cells (*55*). Other studies suggest that
247 TGF-β signaling is required for the alveolar cell plasticity (*36*) and alveolar regeneration (*37*). Our
248 results showed that TGF-β signaling is necessary for AT1 cell regeneration in the context of PPCs.
249 In *Pclaf* KO lung, p-Smad3 was significantly decreased in regenerative alveoli lesions (Fig. 5, F
250 and G) but elevated in inflamed fibrotic lesions (Fig. S12). In line with this, SMAD3-target genes
251 were downregulated in IPF PPCs while upregulated in IPF fibroblasts compared to normal lungs
252 (Fig. 5, O and P, and Fig. S13). Thus, it is highly likely that TGF-β signaling spatiotemporally
253 contributes to lung fibrosis or regeneration, depending on cell types or lesions.

254 The current therapeutic strategy for lung fibrosis has focused on inhibiting fibroblasts using
255 pirfenidone and nintedanib (*56*). Recent studies suggested that failure of lung regeneration is one
256 of the fundamental pathogeneses of lung fibrosis (*7, 9-13*). Intriguingly, disrupted AT2 cell lineage
257 plasticity by *Pclaf* KO drove lung fibrosis rather than lung regeneration (Fig. 2). Based on our
258 findings, we identified PCLAF-activation–mimicking drugs and validated their therapeutic impact
259 on lung regeneration in vivo and in vitro (Fig. 6). This strategy, which facilitates the repopulation
260 of functional lung epithelial cells, may be an alternative regimen or preventive measure for lung
261 fibrosis caused by thoracic radiotherapy in lung cancer patients.

262 The *Pclaf* KO mice showed slight alteration of immune cell status (*57*). Since immune cells
263 also play an essential role in lung regeneration and disease (*58*), the impact of *Pclaf* KO on immune
264 cells may contribute to the lung regeneration phenotype. Nonetheless, consistent with the *Pclaf*
265 KO mouse phenotype, the results from lung organoids without immunocytes suggest that the role
266 of the PCLAF-DREAM axis in lung epithelial cell plasticity is independent of immune cells.
267 Although mouse and organoid models have been extensively employed to study lung
268 pathophysiology, our finding in murine systems remains to be tested in a human-relevant system,
269 such as human lung organoids.

270 Together, our comprehensive approaches reveal a new role of the PCLAF-DREAM axis in
271 driving alveolar cell plasticity via CLIC4-TGF-β for lung regeneration. Furthermore, this study
272 suggests that phenelzine, a drug mimicking the PCLAF-DREAM transcriptional signature, may
273 be a viable therapeutic option for lung disease.

274

Acknowledgments

We are grateful to Pierre D. McCrea and Malgorzata Kloc for insightful comments; Joel M. Sederstrom for technical assistance; Stuart H. Yuspa (Center for Cancer Research, NCI) for reagents (pAltermax-3HA-CLIC4); Ann Sutton (Research Medical Library, MD Anderson) for editing the manuscript. This work was supported by the Cancer Prevention and Research Institute of Texas (RP200315 to J.-I.P.), the National Cancer Institute (CA193297 and CA256207 to J.-I.P.), an Institutional Research Grant (MD Anderson to J.-I.P.), Specialized Program of Research Excellence (SPORE) grant in endometrial cancer (P50 CA83639), and Radiation Oncology Research Initiatives. The core facilities at MD Anderson (DNA sequencing and Genetically Engineered Mouse Facility) were supported by National Cancer Institute Cancer Center Support Grant (P30 CA016672 to MD Anderson). The core facilities at Baylor College of Medicine (Cytometry & Cell Sorting Core and Single Cell Genomics Core) were supported by CPRIT (RP180672, RP200504) and the National Institutes of Health (CA125123, RR024574).

Author contributions

Conceptualization: B.K. and J.-I.P.; Methodology: B.K., L.V.E., K.-S.P., J.C., M.P., C.K., and J.-I.P.; Validation: B.K. and J.-I.P.; Formal analysis: B.K. and J.-I.P.; Investigation: B.K., Y.H., K.-P.K., S.Z., G.Z., J.Z., M.J.K., S.J., and J.-I.P.; Data Curation: B.K., D.L., and J.C.; Visualization: B.K. and J.-I.P.; Supervision: J.-I.P.; Project administration: B.K. and J.-I.P.; Funding acquisition: J.-I.P.; Writing - Original Draft: B.K. and J.-I.P.

Competing interests: All authors declare that they have no competing interests.

Data and material availability

Data availability

Bulk and scRNA-seq data are available via the Gene Expression Omnibus (GSE205815; https://www.ncbi.nlm.nih.gov/geo/query/acc.cgi?acc=GSE205815).
(Log-in token for reviewers: ____)

Code availability

The code used to reproduce the analyses described in this manuscript can be accessed via GitHub (https://github.com/jaeilparklab/Pclaf_lung_regeneration) and will also be available upon request.

Materials and methods

Mice

All mouse experiments were approved by the MD Anderson Institutional Animal Care and Use Committee and performed under MD Anderson guidelines and the Association for Assessment and Accreditation of Laboratory Animal Care international standards. *Pclaf* KO mice from a previously established model (*21*) were used. The *Pclaf-lacZ* knock-in strain was generated by breeding *Pclaf-lacZ-neo* mice with *Rosa26-Cre* driver mice. The *Pclaf-lacZ-neo* strain was established by in vitro fertilization of the sperm carrying the Pclaf-lacZ-neo targeted allele (C57BL/6N-A^{tm1Brd} Pclaf$^{tm1a(EUCOMM)Wtsi}$/WtsiPh; EMMA ID: EM:09820). The targeted or recombinant alleles were validated by genomic DNA PCR and Sanger sequencing.

Bleomycin-induced lung injury

Eight to ten-week-old mice were anesthetized via inhalation of isoflurane using a calibrated vaporizer for approximately 3 mins. The mice were positioned on the intratracheal intubation stand and intubated IV catheters (22GA × 1.00 IN, 0.9 × 25 mm; BD, NJ) in the trachea using BioLite (Biotex, TX) intubation system with optic fiber. The intubated mice were given 1.25 U/kg of bleomycin in 50 µl of PBS. One day before the injury, the blood arterial oxygen saturation and breath rate per minute were recorded using a small rodent oximeter sensor mounted on the thigh of each tested mouse (MouseOX; STARR Life Sciences, Oakmont, PA) every other day. Data were collected for a minimum of 10 seconds with no error code. The mice were euthanized at the acute injury phase (3 days after injury [dpi], regeneration phase [7 dpi], and chronic fibrotic phase [21 dpi]) for post-mortem lung tissue collection, followed by histology.

Histology and immunohistochemistry

Lung tissues were perfused with cold phosphate-buffered saline (PBS, pH 7.4) into the right ventricle, fixed with 10% formalin, embedded in paraffin, and sectioned at 5-µm thickness. The sections were stained with hematoxylin and eosin for histological analysis. For picrosirius red staining, deparaffinized and hydrated sections were stained with picrosirius red solution (0.1% Direct Red 80 [Sigma] in saturated [1.3%] picric acid) for 1 hr. Sections were washed with 0.5% acetic acid and dehydrated before mounting. For the immunohistochemistry analysis, sections were immunostained according to standard protocols(*19*). For antigen retrieval, sections were subjected to heat-induced epitope retrieval pre-treatment at 120 °C using citrate-based antigen unmasking solution (Vector Laboratories, Burlingame, CA, USA), tris-based antigen unmasking solution (Vector Laboratories), or universal antigen retrieval reagent (R&D System). Specific information on antibodies is described in Data file S7.

X-gal staining

Lung tissues were perfused with cold phosphate-buffered saline (PBS, pH 7.4) into the right ventricle, incubated with a mixture of 30% sucrose and 10% optimal cutting temperature (OCT) compound in PBS for 30min at 4 °C, embedded in OCT compound, and sectioned at 10-µm thickness. Frozen lung sections were fixed with 0.2% glutaraldehyde for 10 mins and washed in wash buffer (0.02% IGEPAL CA-630, 0.01% sodium deoxycholate, 2mM $MgCl_2$, 0.1M phosphate buffer pH 7.5) for 10 mins twice. And then slides were incubated with X-gal staining solution (1 mg/ml X-gal, 5mM potassium ferricyanide, 5mM potassium ferrocyanide in wash buffer) for 16 hours in 37 °C. X-gal-stained slides were post-fixed with 4% PFA for 10 min and washed with

350 PBS for 5 mins 3 times. For counterstaining, slides were incubated with nuclear fast red solution
351 (Vector Laboratories, Burlingame, CA, USA) for 2 mins.
352
353 **Lung cell isolation**
354 Lungs were harvested from euthanized mice after perfusing 10 ml of cold PBS into the right
355 ventricle. Lungs were minced after the removal of extra-pulmonary tissues and digested in
356 Leibovitz media (Gibco, USA, no. 21083-027) with 2 mg/ml collagenase type I (Worthington,
357 CLS-1, LS004197), 2 mg/ml elastase (Worthington, ESL, LS002294), and 0.4 mg/ml DNase I
358 (Sigma, DN-25) for 45 min at 37 °C. To stop the digestion, fetal bovine serum (FBS, HyClone;
359 Cytiva) was added to a final concentration of 20%. The digested tissues were sequentially filtered
360 through a 70-µm and a 40-µm cell strainer (Falcon, 352350 and 352340, respectively). The samples
361 were incubated with 1 ml of red blood cell lysis buffer (15 mM NH_4Cl, 12 mM $NaHCO_3$, 0.1 mM
362 EDTA, pH 8.0) for 2 min on ice. Leibovitz with 10% FBS and 1 mM EDTA was used for
363 resuspension and washing for magnetic-activated cell sorting (MACS) or fluorescence-activated
364 cell sorting.
365 For lung epithelial cell isolation, cells were resuspended in 400 µl of buffer with 30 µl of
366 CD31 MicroBeads (130-097-418; Miltenyi Biotec, Bergisch Gladbach, Germany), 30 µl of CD45
367 MicroBeads (130-052-301; Miltenyi Biotec), and 30 µl of anti-Ter-119 MicroBeads (130-049-901;
368 Miltenyi Biotec) and incubated for 30 min at 4 °C, followed by negative selection according to the
369 manufacturer's instructions. Cells were then resuspended with 400 µl of buffer with 30 µl of
370 CD326 (EpCAM) MicroBeads (130-105-958; Miltenyi Biotec) and incubated for 30 min at 4 °C,
371 followed by positive selection according to the manufacturer's instructions. Isolated lung epithelial
372 cells were used for the lung organoid culture. In single-cell RNA sequencing (scRNA-seq),
373 digested lung cells were resuspended in 400 µl of buffer with 5 µl of anti-CD31-FITC (BD
374 Biosciences, CA, USA), 5 µl of anti-CD45-APC (BD Biosciences), and 5 µl of anti-CD326
375 (EpCAM)-PE-Cy7 (BD Biosciences) and incubated for 30 min at 4 °C. Cells were then washed
376 twice, followed by sorting of the epithelial cells by fluorescence-activated cell sorting.
377 For lung endothelial cell (LuEC) isolation, cells were resuspended in 400 µl of buffer with
378 30 µl of CD31 MicroBeads and incubated for 30 min at 4 °C, followed by positive selection
379 according to the manufacturer's instructions. Isolated LuECs were cultured with EC growth media
380 (DMEM; Corning; 10-013-CV, 20% FBS, 1× glu-pen-strep; Gibco, USA; 10378016, 100 µg/ml
381 endothelial cell growth factor (ECGS); Sigma; E2759, 100 µg/ml heparin; Sigma; H3149, 25 mM
382 HEPES) on 0.1% gelatin (Sigma, G1393)-coated plates. Cultured LuECs were then isolated with
383 CD31 MicroBeads and expanded until passage 3. Expanded LuECs were cryopreserved for lung
384 organoid culture.
385
386 **Lung organoid culture**
387 Lung epithelial cells ($Ter119^-/Cd31^-/Cd45^-/Epcam^+$) isolated from 7-10-week-old *Pclaf* WT or
388 *Pclaf* KO mice at 7 dpi of bleomycin were cultured with lung stromal cells in a 3D organoid air-
389 liquid interface, as described previously(*26-28*). In brief, freshly sorted lung epithelial cells were
390 resuspended in 3D organoid media Dulbecco's modified Eagle's medium (DMEM)/F12 (Gibco,
391 USA), 10% fetal bovine serum (FBS; HyClone, USA), 1× penicillin-streptomycin-glutamine
392 (Gibco, USA), and 1X insulin-transferrin-selenium (Sigma)) and mixed with LuECs at a ratio of
393 1:1. Cells containing 3D media were mixed with growth factor-reduced Matrigel (BD Biosciences)
394 at a ratio of 1:1. The 100 µl of mixtures containing lung epithelial cells (5×10^3) and LuECs ($5 \times$
395 10^4) were placed in the transwell insert (0.4-µm pore, Corning, Lowell, MA). After incubation for

396 30 mins at 37°C in an incubator, 500 µl of 3D media were placed in the bottom chamber to generate
397 the liquid-air interface. Media were exchanged every other day, with or without harmine (200 nM;
398 Abcam), phenelzine (10 µM; Cayman, MI, USA), or TGF-β1 (2 ng/ml; R&D System). For viral
399 transduction, freshly isolated lung epithelial cells were resuspended in 500 µl of 3D media
400 containing lentivirus (2.5×10^7 TU/ml) and polybrene (7 µg/ml) and centrifuged for 1 hr at 600 g
401 at 32°C. Cells were incubated at 37°C in an incubator for 7 hours, followed by organoid culture.
402
403 **Gene construct**
404 pLenti-CMV-MSC-RFP-SV-Puro vector was purchased from Addgene (#109377) and used as a
405 control vector or backbone for further cloning. For constructing the pLenti-3HA-Clic4-T2A-GFP
406 plasmid, we prepared a pLenti vector backbone using restriction enzymes, XbaI (NEB, USA) and
407 BamHI (NEB, USA). Three DNA fragments of Kozak-3HA, Clic4, and T2A-GFP were amplified
408 with Phusion High-Fidelity DNA Polymerase (NEB, USA) using pLJC5-Tmem192-3HA
409 (Addgene, #102930) for Kozak-3HA, pAltermax-3HA-Clic4(*39*) for Clic4, and pLenti-CMV-
410 mCherry-T2A-GFP for T2A-GFP. We assembled the pLenti-3HA-Clic4-T2A-GFP vector with
411 pLenti backbone and fragments using NEBuilder HiFi DNA Assembly Master Mix (NEB, USA)
412 according to the manufacturer's instructions. Primer information is described in Supplementary
413 Table 7. We used pLenti-3FLAG -Lin52 (WT or S28A), as previously generated (*19*).
414
415 **Lentivirus preparation**
416 Lentiviruses were produced using 2nd-generation packaging vectors in 293T cells. 293T cells were
417 cultured until 70%-80% confluent, and the media were replaced with antibiotics-free DMEM (10%
418 FBS). After 1 hr of media exchange, cells were transfected with vector mixtures in Opti-MEM
419 (Gibco, USA). To generate a vector mixture, pMD2.G (1.3 pmol), psPAX2 (0.72 pmol), DNA
420 (1.64 pmol), and polyethyleneimine (PEI, 39 µg) were added to 800 µl of Opti-MEM and
421 incubated for 15 mins. After 12 hrs of transfection, the media were exchanged with complete media
422 (DMEM, 10% FBS, and 1X penicillin-streptomycin). The virus supernatant was collected after 24
423 hrs and 48 hrs and filtered with a 0.45-µm syringe filter (Thermo Fisher, CA, USA); polyethylene
424 glycol (PEG) solution (40% PEG-8000 [Thermo Fisher, CA, USA], and 1.2 M NaCl in pH 7.4
425 PBS) were added in a 3:1 ratio. After overnight incubation of the virus-PEG mixture at 4°C, the
426 virus pellet was generated by centrifugation at 1600X g and 4 °C for 1 hr. The pellet was
427 reconstituted in 1 ml of 3D media and incubated for 15 mins at 4 °C. Reconstituted virus was
428 centrifuged at 20,000X g and 4 °C for 3 mins to remove protein debris. The collected virus was
429 stored in a -80 °C freezer. pLenti-RFP, pLenti-3FLAG-Lin52WT, pLenti-3FLAG -Lin52S28A,
430 and pLenti-3HA-Clic4-T2A-GFP vectors were used for lentivirus generation. For virus titration,
431 5×10^5 293T cells were seeded into 48-well plates (Thermo Fisher, CA, USA). After 24 hrs, cells
432 were infected by the serially diluted virus with 10 µg/ml polybrene. After 48 hrs of transfection,
433 virus transduction units per ml (TU/ml) were measured by fluorescence microscopy.
434
435 **Single-cell gene expression library**
436 Freshly isolated lung epithelial cells from *Pclaf* WT and *Pclaf* KO mice at 7 dpi of bleomycin
437 instillation were used to prepare the single-cell RNA library. To generate single-cell gene
438 expression libraries, 1.6×10^4 cells per group of single cells were subjected to the Chromium
439 Single Cell Gene Expression 3v3.1 kit (10X genomics) at the Single Cell Genomics Core at Baylor
440 College of Medicine. In brief, reverse transcription (RT) reagents, gel beads containing barcoded

441 oligonucleotides, and oil were loaded on a chromium controller (×10 Genomics) to generate
442 single-cell gel beads-in-emulsions (GEMs) in which full-length cDNA was synthesized and
443 barcoded for each single-cell. Subsequently, the GEMs were broken, and cDNA from every single
444 cell was pooled. Following clean-up using Dynabeads MyOne Silane Beads, cDNA was amplified
445 by PCR. The amplified product is fragmented to an optimal size before end-repair, A-tailing, and
446 adaptor ligation. The final library was generated by amplification.
447
448 **Single-cell RNA sequencing**
449 Libraries were run on Novaseq for Illumina PE150 sequencing with 20,000 reads per cell. Post-
450 processing and quality control were performed by Novogene using the 10× Cell Ranger package
451 (v. 3.1.0, 10X Genomics). Reads were aligned to the GRCm38 reference assembly using STAR
452 aligner (*59*) (v. 2.7.10a).
453
454 **Single-cell RNA preprocessing and quality control**
455 The Cell Ranger output was used as the input to Seurat v. 4.1.0 for further analysis of the scRNA-
456 seq samples. For each sample, poor-quality cells were filtered based on the number of features
457 (min.features = 200, min.cells = 3), number of RNAs detected (> 200 and < 5000), and percentage
458 of reads arising from the mitochondrial genome (< 20%). We combined *Pclaf* WT and *Pclaf* KO
459 samples using the merge function of Seurat. Clustering using default parameters and uniform
460 manifold approximation and projection (UMAP) non-linear dimensionality reduction were
461 performed using Seurat v. 4.1.0, and we referred to the result as our integrated clusters. The marker
462 genes of each cluster (differentially expressed genes [DEGs] in each cluster compared with all
463 other clusters) and differentially expressed genes between samples were identified with Seurat
464 using the "FindAllMarkers" function with the parameters logfc.threshold = 0.25 and min.pct =
465 0.25. For the lung epithelial cell analysis, we downsized the *Pclaf* KO sample by one-sixth (from
466 10,807 cells to 1,797 cells).
467
468 **Gene set enrichment analysis**
469 The DEGs between *Pclaf* WT vs. *Pclaf* KO in the PPC clusters were identified by the Wilcoxon
470 sum test and AUROC statistics using the Presto package v. 1.0.0. They were then subjected to a
471 gene set enrichment analysis (GSEA) using the fgsea package v. 1.16.0. The curated gene sets (C2)
472 in the Molecular Signature Database (MsigDB) v. 7.5.1 were used for the GSEA using the msigdbr
473 package.
474
475 **Pseudotime trajectory analysis**
476 Velocyto.py was used to estimate the RNA velocities of single cells by distinguishing between
477 unspliced and spliced mRNAs in the standard single-cell RNA-sequencing data (*60*). The BAM
478 files, output from Cell Ranger, were subjected to generate loom files containing three categories:
479 "spliced", "unspliced", and "ambiguous". The loom files were applied to calculate the dynamic
480 velocity graph using scVelo v. 0.2.4 (*61*).
481
482 **Developmental state analysis**
483 CytoTRACE v. 0.3.3 was used to predict the relative differentiation state of a single cell (*62*). The
484 cells were given a CytoTRACE score according to their differentiation potential, with a higher
485 score indicating higher stemness/fewer differential characteristics.
486

487 **Gene regulatory network analysis**
488 For regulon identification, a gene regulatory network analysis was performed using the python
489 version of the SCENIC (pySCENIC) method (v. 0.11.2)[63]. pySCENIC integrates a random forest
490 classifier (GENIE3) (v. 1.0.0) to identify potential TF targets based on their co-expression with
491 RcisTarget (v. 0.99.0) for *cis*-regulatory motif enrichment analysis in the promoter of target genes
492 (±500 bp of the transcription start site) and identify the regulon, which consists of a TF and its co-
493 expressed target genes. The *Mus musculus* 10 (mm10) motif database provided by the pySCENIC
494 authors was used. Finally, for each regulon, pySCENIC uses the AUCell (v. 0.99.5) algorithm to
495 score the regulon activity in each cell (Z score, a standardized AUCell score, was used). All
496 parameters used for running were specified in the original pySCENIC pipeline. The ranking
497 databases used were mm10-refseq-r80-10 kb-up-and-down-tss.mc9nr.feather mm10-refseq-r80-
498 500bp-up-and-100bp-down-tss.mc9nr.feather, which were downloaded from
499 https://resources.aertslab.org/cistarget/. The motif database was downloaded from
500 https://resources.aertslab.org/cistarget/motif2tf/.
501
502 **Public scRNA-seq data analysis**
503 A public scRNA-seq data set (GSE141259)(*30*), generated by subjecting sorted cells from the
504 mouse lung epithelial compartment at 18 different time points after bleomycin instillation, was
505 analyzed according to the code provided in the original study. A public scRNA-seq data set
506 (GSE135893)(*52*) was generated from the cells of 20 pulmonary fibrosis and 10 control human
507 lungs and analyzed according to the code provided in the original study.
508
509 **Gene expression analysis by qRT-PCR**
510 RNAs were extracted by TRIzol (Invitrogen) and used to synthesize cDNAs using the iScript
511 cDNA synthesis kit (Biorad). qRT-PCR was performed using an Applied Biosystems 7500 Real-
512 Time PCR machine with the primers listed in Supplementary Table 7. Target gene expression was
513 normalized to that of mouse *Hprt1*. Comparative $2^{-\Delta\Delta Ct}$ methods were used to quantify qRT-PCR
514 results.

515 **References**
516

517 1. H. B. Schiller, D. T. Montoro, L. M. Simon, E. L. Rawlins, K. B. Meyer, M. Strunz, F. A.
518 Vieira Braga, W. Timens, G. H. Koppelman, G. R. S. Budinger, J. K. Burgess, A.
519 Waghray, M. van den Berge, F. J. Theis, A. Regev, N. Kaminski, J. Rajagopal, S. A.
520 Teichmann, A. V. Misharin, M. C. Nawijn, The Human Lung Cell Atlas: A High-
521 Resolution Reference Map of the Human Lung in Health and Disease. *Am J Respir Cell*
522 *Mol Biol* **61**, 31-41 (2019).
523 2. M. N. Chonghaile, B. D. Higgins, J. Costello, J. G. Laffey, Hypercapnic acidosis
524 attenuates lung injury induced by established bacterial pneumonia. *Anesthesiology* **109**,
525 837-848 (2008).
526 3. R. Kc, S. D. Shukla, S. S. Gautam, P. M. Hansbro, R. F. O'Toole, The role of
527 environmental exposure to non-cigarette smoke in lung disease. *Clin Transl Med* **7**, 39
528 (2018).
529 4. G. Raghu, H. R. Collard, J. J. Egan, F. J. Martinez, J. Behr, K. K. Brown, T. V. Colby, J.
530 F. Cordier, K. R. Flaherty, J. A. Lasky, D. A. Lynch, J. H. Ryu, J. J. Swigris, A. U.
531 Wells, J. Ancochea, D. Bouros, C. Carvalho, U. Costabel, M. Ebina, D. M. Hansell, T.
532 Johkoh, D. S. Kim, T. E. King, Jr., Y. Kondoh, J. Myers, N. L. Müller, A. G. Nicholson,
533 L. Richeldi, M. Selman, R. F. Dudden, B. S. Griss, S. L. Protzko, H. J. Schünemann, An
534 official ATS/ERS/JRS/ALAT statement: idiopathic pulmonary fibrosis: evidence-based
535 guidelines for diagnosis and management. *Am J Respir Crit Care Med* **183**, 788-824
536 (2011).
537 5. D. N. Kotton, E. E. Morrisey, Lung regeneration: mechanisms, applications and emerging
538 stem cell populations. *Nat Med* **20**, 822-832 (2014).
539 6. M. C. Melo-Narváez, J. Stegmayr, D. E. Wagner, M. Lehmann, Lung regeneration:
540 implications of the diseased niche and ageing. *Eur Respir Rev* **29**, (2020).
541 7. J. Liang, Y. Zhang, T. Xie, N. Liu, H. Chen, Y. Geng, A. Kurkciyan, J. M. Mena, B. R.
542 Stripp, D. Jiang, P. W. Noble, Hyaluronan and TLR4 promote surfactant-protein-C-
543 positive alveolar progenitor cell renewal and prevent severe pulmonary fibrosis in mice.
544 *Nature Medicine* **22**, 1285-1293 (2016).
545 8. Y. Kobayashi, A. Tata, A. Konkimalla, H. Katsura, R. F. Lee, J. Ou, N. E. Banovich, J.
546 A. Kropski, P. R. Tata, Persistence of a regeneration-associated, transitional alveolar
547 epithelial cell state in pulmonary fibrosis. *Nature Cell Biology* **22**, 934-946 (2020).
548 9. J. Katzen, B. D. Wagner, A. Venosa, M. Kopp, Y. Tomer, S. J. Russo, A. C. Headen, M.
549 C. Basil, J. M. Stark, S. Mulugeta, R. R. Deterding, M. F. Beers, An SFTPC BRICHOS
550 mutant links epithelial ER stress and spontaneous lung fibrosis. *JCI Insight* **4**, (2019).
551 10. R. P. Naikawadi, S. Disayabutr, B. Mallavia, M. L. Donne, G. Green, J. L. La, J. R.
552 Rock, M. R. Looney, P. J. Wolters, Telomere dysfunction in alveolar epithelial cells
553 causes lung remodeling and fibrosis. *JCI Insight* **1**, e86704 (2016).
554 11. S. I. Nureki, Y. Tomer, A. Venosa, J. Katzen, S. J. Russo, S. Jamil, M. Barrett, V.
555 Nguyen, M. Kopp, S. Mulugeta, M. F. Beers, Expression of mutant Sftpc in murine
556 alveolar epithelia drives spontaneous lung fibrosis. *J Clin Invest* **128**, 4008-4024 (2018).
557 12. P. A. Reyfman, J. M. Walter, N. Joshi, K. R. Anekalla, A. C. McQuattie-Pimentel, S.
558 Chiu, R. Fernandez, M. Akbarpour, C. I. Chen, Z. Ren, R. Verma, H. Abdala-Valencia,
559 K. Nam, M. Chi, S. Han, F. J. Gonzalez-Gonzalez, S. Soberanes, S. Watanabe, K. J. N.
560 Williams, A. S. Flozak, T. T. Nicholson, V. K. Morgan, D. R. Winter, M. Hinchcliff, C.

561 L. Hrusch, R. D. Guzy, C. A. Bonham, A. I. Sperling, R. Bag, R. B. Hamanaka, G. M.
562 Mutlu, A. V. Yeldandi, S. A. Marshall, A. Shilatifard, L. A. N. Amaral, H. Perlman, J. I.
563 Sznajder, A. C. Argento, C. T. Gillespie, J. Dematte, M. Jain, B. D. Singer, K. M. Ridge,
564 A. P. Lam, A. Bharat, S. M. Bhorade, C. J. Gottardi, G. R. S. Budinger, A. V. Misharin,
565 Single-Cell Transcriptomic Analysis of Human Lung Provides Insights into the
566 Pathobiology of Pulmonary Fibrosis. *Am J Respir Crit Care Med* **199**, 1517-1536 (2019).
567 13. H. Wu, Y. Yu, H. Huang, Y. Hu, S. Fu, Z. Wang, M. Shi, X. Zhao, J. Yuan, J. Li, X.
568 Yang, E. Bin, D. Wei, H. Zhang, J. Zhang, C. Yang, T. Cai, H. Dai, J. Chen, N. Tang,
569 Progressive pulmonary fibrosis is caused by elevated mechanical tension on alveolar
570 stem cells. *Cell* **184**, 845-846 (2021).
571 14. M. M. Harrison, C. J. Ceol, X. W. Lu, H. R. Horvitz, Some C. elegans class B synthetic
572 multivulva proteins encode a conserved LIN-35 Rb-containing complex distinct from a
573 NuRD-like complex. *Proc. Natl. Acad. Sci. U. S. A.* **103**, 16782-16787 (2006).
574 15. M. Korenjak, B. Taylor-Harding, U. K. Binne, J. S. Satterlee, O. Stevaux, R. Aasland, H.
575 White-Cooper, N. Dyson, A. Brehm, Native E2F/RBF complexes contain Myb-
576 interacting proteins and repress transcription of developmentally controlled E2F target
577 genes. *Cell* **119**, 181-193 (2004).
578 16. P. W. Lewis, E. L. Beall, T. C. Fleischer, D. Georlette, A. J. Link, M. R. Botchan,
579 Identification of a Drosophila Myb-E2F2/RBF transcriptional repressor complex. *Genes*
580 *Dev.* **18**, 2929-2940 (2004).
581 17. L. Litovchick, S. Sadasivam, L. Florens, X. P. Zhu, S. K. Swanson, S. Velmurugan, R. S.
582 Chen, M. P. Washburn, X. S. Liu, J. A. DeCaprio, Evolutionarily conserved multisubunit
583 RBL2/p130 and E2F4 protein complex represses human cell cycle-dependent genes in
584 quiescence. *Mol. Cell* **26**, 539-551 (2007).
585 18. S. Sadasivam, S. H. Duan, J. A. DeCaprio, The MuvB complex sequentially recruits B-
586 Myb and FoxM1 to promote mitotic gene expression. *Genes Dev.* **26**, 474-489 (2012).
587 19. M. J. Kim, C. Cervantes, Y. S. Jung, X. Zhang, J. Zhang, S. H. Lee, S. Jun, L.
588 Litovchick, W. Wang, J. Chen, B. Fang, J. I. Park, PAF remodels the DREAM complex
589 to bypass cell quiescence and promote lung tumorigenesis. *Mol Cell* **81**, 1698-
590 1714.e1696 (2021).
591 20. X. Wang, Y. S. Jung, S. Jun, S. Lee, W. Q. Wang, A. Schneider, Y. S. Oh, S. H. Lin, B.
592 J. Park, J. J. Chen, K. Keyomarsi, J. I. Park, PAF-Wnt signaling-induced cell plasticity is
593 required for maintenance of breast cancer cell stemness. *Nat. Commun.* **7**, 13 (2016).
594 21. M. J. Kim, B. Xia, H. N. Suh, S. H. Lee, S. Jun, E. M. Lien, J. Zhang, K. F. Chen, J. I.
595 Park, PAF-Myc-Controlled Cell Stemness Is Required for Intestinal Regeneration and
596 Tumorigenesis. *Dev. Cell* **44**, 582-+ (2018).
597 22. A. Moeller, K. Ask, D. Warburton, J. Gauldie, M. Kolb, The bleomycin animal model: a
598 useful tool to investigate treatment options for idiopathic pulmonary fibrosis? *Int J*
599 *Biochem Cell Biol* **40**, 362-382 (2008).
600 23. Y. Kobayashi, A. Tata, A. Konkimalla, H. Katsura, R. F. Lee, J. Ou, N. E. Banovich, J.
601 A. Kropski, P. R. Tata, Persistence of a regeneration-associated, transitional alveolar
602 epithelial cell state in pulmonary fibrosis. *Nat Cell Biol* **22**, 934-946 (2020).
603 24. T. Sun, Z. Huang, H. Zhang, C. Posner, G. Jia, T. R. Ramalingam, M. Xu, H. Brightbill,
604 J. G. Egen, A. Dey, J. R. Arron, TAZ is required for lung alveolar epithelial cell
605 differentiation after injury. *JCI Insight* **5**, (2019).

606 25. C. E. Barkauskas, M. J. Cronce, C. R. Rackley, E. J. Bowie, D. R. Keene, B. R. Stripp, S.
607 H. Randell, P. W. Noble, B. L. Hogan, Type 2 alveolar cells are stem cells in adult lung.
608 *J Clin Invest* **123**, 3025-3036 (2013).
609 26. J. H. Lee, D. H. Bhang, A. Beede, T. L. Huang, B. R. Stripp, K. D. Bloch, A. J. Wagers,
610 Y. H. Tseng, S. Ryeom, C. F. Kim, Lung stem cell differentiation in mice directed by
611 endothelial cells via a BMP4-NFATc1-thrombospondin-1 axis. *Cell* **156**, 440-455 (2014).
612 27. A. F. M. Dost, A. L. Moye, M. Vedaie, L. M. Tran, E. Fung, D. Heinze, C. Villacorta-
613 Martin, J. Huang, R. Hekman, J. H. Kwan, B. C. Blum, S. M. Louie, S. P. Rowbotham, J.
614 Sainz de Aja, M. E. Piper, P. J. Bhetariya, R. T. Bronson, A. Emili, G. Mostoslavsky, G.
615 A. Fishbein, W. D. Wallace, K. Krysan, S. M. Dubinett, J. Yanagawa, D. N. Kotton, C. F.
616 Kim, Organoids Model Transcriptional Hallmarks of Oncogenic KRAS Activation in
617 Lung Epithelial Progenitor Cells. *Cell Stem Cell* **27**, 663-678.e668 (2020).
618 28. K. T. Leeman, P. Pessina, J. H. Lee, C. F. Kim, Mesenchymal Stem Cells Increase
619 Alveolar Differentiation in Lung Progenitor Organoid Cultures. *Sci Rep* **9**, 6479 (2019).
620 29. J. Choi, J. E. Park, G. Tsagkogeorga, M. Yanagita, B. K. Koo, N. Han, J. H. Lee,
621 Inflammatory Signals Induce AT2 Cell-Derived Damage-Associated Transient
622 Progenitors that Mediate Alveolar Regeneration. *Cell Stem Cell* **27**, 366-382.e367 (2020).
623 30. M. Strunz, L. M. Simon, M. Ansari, J. J. Kathiriya, I. Angelidis, C. H. Mayr, G.
624 Tsidiridis, M. Lange, L. F. Mattner, M. Yee, P. Ogar, A. Sengupta, I. Kukhtevich, R.
625 Schneider, Z. Zhao, C. Voss, T. Stoeger, J. H. L. Neumann, A. Hilgendorff, J. Behr, M.
626 O'Reilly, M. Lehmann, G. Burgstaller, M. Königshoff, H. A. Chapman, F. J. Theis, H. B.
627 Schiller, Alveolar regeneration through a Krt8+ transitional stem cell state that persists in
628 human lung fibrosis. *Nat Commun* **11**, 3559 (2020).
629 31. N. Göckler, G. Jofre, C. Papadopoulos, U. Soppa, F. J. Tejedor, W. Becker, Harmine
630 specifically inhibits protein kinase DYRK1A and interferes with neurite formation. *Febs j*
631 **276**, 6324-6337 (2009).
632 32. C. Forristal, S. A. Henley, J. I. MacDonald, J. R. Bush, C. Ort, D. T. Passos, S. Talluri, C.
633 A. Ishak, M. J. Thwaites, C. J. Norley, L. Litovchick, J. A. DeCaprio, G. DiMattia, D. W.
634 Holdsworth, F. Beier, F. A. Dick, Loss of the mammalian DREAM complex deregulates
635 chondrocyte proliferation. *Mol Cell Biol* **34**, 2221-2234 (2014).
636 33. A. N. Nabhan, D. G. Brownfield, P. B. Harbury, M. A. Krasnow, T. J. Desai, Single-cell
637 Wnt signaling niches maintain stemness of alveolar type 2 cells. *Science* **359**, 1118-1123
638 (2018).
639 34. H. Y. Jung, S. Jun, M. Lee, H. C. Kim, X. Wang, H. Ji, P. D. McCrea, J. I. Park, PAF and
640 EZH2 Induce Wnt/beta-Catenin Signaling Hyperactivation. *Mol. Cell* **52**, 193-205
641 (2013).
642 35. J. J. Kathiriya, A. N. Brumwell, J. R. Jackson, X. Tang, H. A. Chapman, Distinct Airway
643 Epithelial Stem Cells Hide among Club Cells but Mobilize to Promote Alveolar
644 Regeneration. *Cell Stem Cell* **26**, 346-358.e344 (2020).
645 36. L. Zhao, M. Yee, M. A. O'Reilly, Transdifferentiation of alveolar epithelial type II to
646 type I cells is controlled by opposing TGF-β and BMP signaling. *Am J Physiol Lung Cell*
647 *Mol Physiol* **305**, L409-418 (2013).
648 37. K. A. Riemondy, N. L. Jansing, P. Jiang, E. F. Redente, A. E. Gillen, R. Fu, A. J. Miller,
649 J. R. Spence, A. N. Gerber, J. R. Hesselberth, R. L. Zemans, Single cell RNA sequencing
650 identifies TGFβ as a key regenerative cue following LPS-induced lung injury. *JCI Insight*
651 **5**, (2019).

652 38. A. Shukla, M. Malik, C. Cataisson, Y. Ho, T. Friesen, K. S. Suh, S. H. Yuspa, TGF-beta
653 signalling is regulated by Schnurri-2-dependent nuclear translocation of CLIC4 and
654 consequent stabilization of phospho-Smad2 and 3. *Nat Cell Biol* **11**, 777-784 (2009).
655 39. A. Shukla, S. H. Yuspa, CLIC4 and Schnurri-2: a dynamic duo in TGF-beta signaling
656 with broader implications in cellular homeostasis and disease. *Nucleus* **1**, 144-149 (2010).
657 40. Y. Zhang, D. Handley, T. Kaplan, H. Yu, A. S. Bais, T. Richards, K. V. Pandit, Q. Zeng,
658 P. V. Benos, N. Friedman, O. Eickelberg, N. Kaminski, High throughput determination
659 of TGFβ1/SMAD3 targets in A549 lung epithelial cells. *PLoS One* **6**, e20319 (2011).
660 41. A. C. Mullen, D. A. Orlando, J. J. Newman, J. Lovén, R. M. Kumar, S. Bilodeau, J.
661 Reddy, M. G. Guenther, R. P. DeKoter, R. A. Young, Master transcription factors
662 determine cell-type-specific responses to TGF-β signaling. *Cell* **147**, 565-576 (2011).
663 42. U. Bartram, C. P. Speer, The role of transforming growth factor beta in lung development
664 and disease. *Chest* **125**, 754-765 (2004).
665 43. A. Subramanian, R. Narayan, S. M. Corsello, D. D. Peck, T. E. Natoli, X. Lu, J. Gould, J.
666 F. Davis, A. A. Tubelli, J. K. Asiedu, D. L. Lahr, J. E. Hirschman, Z. Liu, M. Donahue,
667 B. Julian, M. Khan, D. Wadden, I. C. Smith, D. Lam, A. Liberzon, C. Toder, M. Bagul,
668 M. Orzechowski, O. M. Enache, F. Piccioni, S. A. Johnson, N. J. Lyons, A. H. Berger, A.
669 F. Shamji, A. N. Brooks, A. Vrcic, C. Flynn, J. Rosains, D. Y. Takeda, R. Hu, D.
670 Davison, J. Lamb, K. Ardlie, L. Hogstrom, P. Greenside, N. S. Gray, P. A. Clemons, S.
671 Silver, X. Wu, W. N. Zhao, W. Read-Button, X. Wu, S. J. Haggarty, L. V. Ronco, J. S.
672 Boehm, S. L. Schreiber, J. G. Doench, J. A. Bittker, D. E. Root, B. Wong, T. R. Golub, A
673 Next Generation Connectivity Map: L1000 Platform and the First 1,000,000 Profiles.
674 *Cell* **171**, 1437-1452.e1417 (2017).
675 44. M. I. Chung, M. Bujnis, C. E. Barkauskas, Y. Kobayashi, B. L. M. Hogan, Niche-
676 mediated BMP/SMAD signaling regulates lung alveolar stem cell proliferation and
677 differentiation. *Development* **145**, (2018).
678 45. R. LaCanna, D. Liccardo, P. Zhang, L. Tragesser, Y. Wang, T. Cao, H. A. Chapman, E.
679 E. Morrisey, H. Shen, W. J. Koch, B. Kosmider, M. R. Wolfson, Y. Tian, Yap/Taz
680 regulate alveolar regeneration and resolution of lung inflammation. *J Clin Invest* **129**,
681 2107-2122 (2019).
682 46. S. Sadasivam, J. A. DeCaprio, The DREAM complex: master coordinator of cell cycle-
683 dependent gene expression. *Nat. Rev. Cancer* **13**, 585-595 (2013).
684 47. N. N. Rashid, R. Yusof, R. J. Watson, Disruption of repressive p130-DREAM complexes
685 by human papillomavirus 16 E6/E7 oncoproteins is required for cell-cycle progression in
686 cervical cancer cells. *J. Gen. Virol.* **92**, 2620-2627 (2011).
687 48. L. Litovchick, L. A. Florens, S. K. Swanson, M. P. Washburn, J. A. DeCaprio, DYRK1A
688 protein kinase promotes quiescence and senescence through DREAM complex assembly.
689 *Genes Dev.* **25**, 801-813 (2011).
690 49. M. L. Beshiri, K. B. Holmes, W. F. Richter, S. Hess, A. Islam, Q. Yan, L. Plante, L.
691 Litovchick, N. Gevry, N. Lopez-Bigas, W. G. Kaelin, E. V. Benevolenskaya,
692 Coordinated repression of cell cycle genes by KDM5A and E2F4 during differentiation.
693 *Proc. Natl. Acad. Sci. U. S. A.* **109**, 18499-18504 (2012).
694 50. M. Fischer, P. Grossmann, M. Padi, J. A. DeCaprio, Integration of TP53, DREAM,
695 MMB-FOXM1 and RB-E2F target gene analyses identifies cell cycle gene regulatory
696 networks. *Nucleic Acids Res.* **44**, 6070-6086 (2016).

697 51. H. Walston, A. N. Iness, L. Litovchick, DREAM On: Cell Cycle Control in Development
698 and Disease. *Annu Rev Genet* **55**, 309-329 (2021).
699 52. A. C. Habermann, A. J. Gutierrez, L. T. Bui, S. L. Yahn, N. I. Winters, C. L. Calvi, L.
700 Peter, M. I. Chung, C. J. Taylor, C. Jetter, L. Raju, J. Roberson, G. Ding, L. Wood, J. M.
701 S. Sucre, B. W. Richmond, A. P. Serezani, W. J. McDonnell, S. B. Mallal, M. J.
702 Bacchetta, J. E. Loyd, C. M. Shaver, L. B. Ware, R. Bremner, R. Walia, T. S. Blackwell,
703 N. E. Banovich, J. A. Kropski, Single-cell RNA sequencing reveals profibrotic roles of
704 distinct epithelial and mesenchymal lineages in pulmonary fibrosis. *Sci Adv* **6**, eaba1972
705 (2020).
706 53. P. Kadur Lakshminarasimha Murthy, V. Sontake, A. Tata, Y. Kobayashi, L. Macadlo, K.
707 Okuda, A. S. Conchola, S. Nakano, S. Gregory, L. A. Miller, J. R. Spence, J. F.
708 Engelhardt, R. C. Boucher, J. R. Rock, S. H. Randell, P. R. Tata, Human distal lung maps
709 and lineage hierarchies reveal a bipotent progenitor. *Nature* **604**, 111-119 (2022).
710 54. N. Frangogiannis, Transforming growth factor-β in tissue fibrosis. *J Exp Med* **217**,
711 e20190103 (2020).
712 55. B. C. Willis, J. M. Liebler, K. Luby-Phelps, A. G. Nicholson, E. D. Crandall, R. M. du
713 Bois, Z. Borok, Induction of epithelial-mesenchymal transition in alveolar epithelial cells
714 by transforming growth factor-beta1: potential role in idiopathic pulmonary fibrosis. *Am*
715 *J Pathol* **166**, 1321-1332 (2005).
716 56. M. Wijsenbeek, V. Cottin, Spectrum of Fibrotic Lung Diseases. *N Engl J Med* **383**, 958-
717 968 (2020).
718 57. Y. M. Amrani, J. Gill, A. Matevossian, E. S. Alonzo, C. Yang, J. H. Shieh, M. A. Moore,
719 C. Y. Park, D. B. Sant'Angelo, L. K. Denzin, The Paf oncogene is essential for
720 hematopoietic stem cell function and development. *J Exp Med* **208**, 1757-1765 (2011).
721 58. F. J. Martinez, H. R. Collard, A. Pardo, G. Raghu, L. Richeldi, M. Selman, J. J. Swigris,
722 H. Taniguchi, A. U. Wells, Idiopathic pulmonary fibrosis. *Nature Reviews Disease*
723 *Primers* **3**, 17074 (2017).
724 59. A. Dobin, C. A. Davis, F. Schlesinger, J. Drenkow, C. Zaleski, S. Jha, P. Batut, M.
725 Chaisson, T. R. Gingeras, STAR: ultrafast universal RNA-seq aligner. *Bioinformatics* **29**,
726 15-21 (2013).
727 60. G. La Manno, R. Soldatov, A. Zeisel, E. Braun, H. Hochgerner, V. Petukhov, K.
728 Lidschreiber, M. E. Kastriti, P. Lönnerberg, A. Furlan, J. Fan, L. E. Borm, Z. Liu, D. van
729 Bruggen, J. Guo, X. He, R. Barker, E. Sundström, G. Castelo-Branco, P. Cramer, I.
730 Adameyko, S. Linnarsson, P. V. Kharchenko, RNA velocity of single cells. *Nature* **560**,
731 494-498 (2018).
732 61. V. Bergen, M. Lange, S. Peidli, F. A. Wolf, F. J. Theis, Generalizing RNA velocity to
733 transient cell states through dynamical modeling. *Nat Biotechnol* **38**, 1408-1414 (2020).
734 62. G. S. Gulati, S. S. Sikandar, D. J. Wesche, A. Manjunath, A. Bharadwaj, M. J. Berger, F.
735 Ilagan, A. H. Kuo, R. W. Hsieh, S. Cai, M. Zabala, F. A. Scheeren, N. A. Lobo, D. Qian,
736 F. B. Yu, F. M. Dirbas, M. F. Clarke, A. M. Newman, Single-cell transcriptional diversity
737 is a hallmark of developmental potential. *Science* **367**, 405-411 (2020).
738 63. B. Van de Sande, C. Flerin, K. Davie, M. De Waegeneer, G. Hulselmans, S. Aibar, R.
739 Seurinck, W. Saelens, R. Cannoodt, Q. Rouchon, T. Verbeiren, D. De Maeyer, J.
740 Reumers, Y. Saeys, S. Aerts, A scalable SCENIC workflow for single-cell gene
741 regulatory network analysis. *Nat Protoc* **15**, 2247-2276 (2020).
742

743 **List of Supplementary Materials**
744
745
746 **Fig. S1 to Fig. S14**
747
748 **Data file S1. Marker genes of each cell type in mouse lung scRNA-seq data.**
749 The list of marker genes for each cell type identity of mouse lung scRNA-seq data (GSE1412259),
750 analyzed by the 'FindAllMarkers' function of Seurat.
751
752 **Data file S2. Marker genes of each cell type in human lung scRNA-seq.**
753 The list of marker genes for each cell type identity of human lung scRNA-seq data (GSE135893),
754 analyzed by the 'FindAllMarkers' function of Seurat.
755
756 **Data file S3. Marker genes of each cell type in mouse lung scRNA-seq from *Pclaf* WT and**
757 ***Pclaf* KO mice at 7 dpi of bleomycin.**
758 The list of marker genes for each cell type identity of *Pclaf* WT and KO mouse lung epithelial
759 cells (collected from mice at 7 dpi of bleomycin instillation), analyzed by 'FindAllMarkers'
760 function of Seurat.
761
762 **Data file S4. List of gene sets from of input into CLUE database.**
763 The list of gene sets of input into the CLUE database (*64*). Gene sets of the PPCs (*Pclaf* WT vs.
764 *Pclaf* KO scRNA-seq shown in Figure 2). Gene sets of KP cells (*shPclaf* vs. *shControl [shCon]*)
765 and H1792 cells (*shPCLAF* vs. *shControl [shCon]*) were identified from the bulk RNA-seq data
766 (GSE136571 and GSE147305, respectively).
767
768 **Data file S5. List of drug candidates identified from the CLUE database.**
769 This spreadsheet has the output of the CLUE database with each gene sets. Each output was
770 derived from the input gene sets listed in Supplementary Table 4; gene sets of PPCs (*Pclaf* WT vs.
771 *Pclaf* KO), KP cells (*shPclaf* vs. *shControl [shCon]*) and H1792 cells (*shPCLAF* vs. *shControl*
772 *[shCon]*). CLUE outputs (drug candidates) with scores higher than 1.5 were selected.
773
774 **Data file S6. Gene ontology of DREAM-target genes generated from the PANTHER database.**
775 The list of gene ontology (GO) (molecular function) of DREAM-target genes analyzed by the
776 PANTHER db (*65*). The gene set of DREAM-target genes (968 genes;
777 FISCHER_DREAM_TARGETS) was analyzed for the statistical overrepresentation test of GO
778 molecular function complete.
779
780 **Data file S7. Antibody and primer information.**
781 This spreadsheet has all information related to antibodies (manufacturers, catalog numbers,
782 dilution rates, and antigen retrieval methods) and primers (sequences for cloning and mRNA
783 quantification).
784
785
786 **Supplementary References**
787

64. A. Subramanian, R. Narayan, S. M. Corsello, D. D. Peck, T. E. Natoli, X. D. Lu, J. Gould, J. F. Davis, A. A. Tubelli, J. K. Asiedu, D. L. Lahr, J. E. Hirschman, Z. H. Liu, M. Donahue, B. Julian, M. Khan, D. Wadden, I. C. Smith, D. Lam, A. Liberzon, C. Toder, M. Bagul, M. Orzechowski, O. M. Enache, F. Piccioni, S. A. Johnson, N. J. Lyons, A. H. Berger, A. F. Shamji, A. N. Brooks, A. Vrcic, C. Flynn, J. Rosains, D. Y. Takeda, R. Hu, D. Davison, J. Lamb, K. Ardlie, L. Hogstrom, P. Greenside, N. S. Gray, P. A. Clemons, S. Silver, X. Y. Wu, W. N. Zhao, W. Read-Button, X. H. Wu, S. J. Haggarty, L. V. Ronco, J. S. Boehm, S. L. Schreiber, J. G. Doench, J. A. Bittker, D. E. Root, B. Wong, T. R. Golub, A Next Generation Connectivity Map: L1000 Platform and the First 1,000,000 Profiles. *Cell* **171**, 1437-+ (2017).

65. H. Mi, A. Muruganujan, X. Huang, D. Ebert, C. Mills, X. Guo, P. D. Thomas, Protocol Update for large-scale genome and gene function analysis with the PANTHER classification system (v.14.0). *Nat Protoc* **14**, 703-721 (2019).

Fig. 1

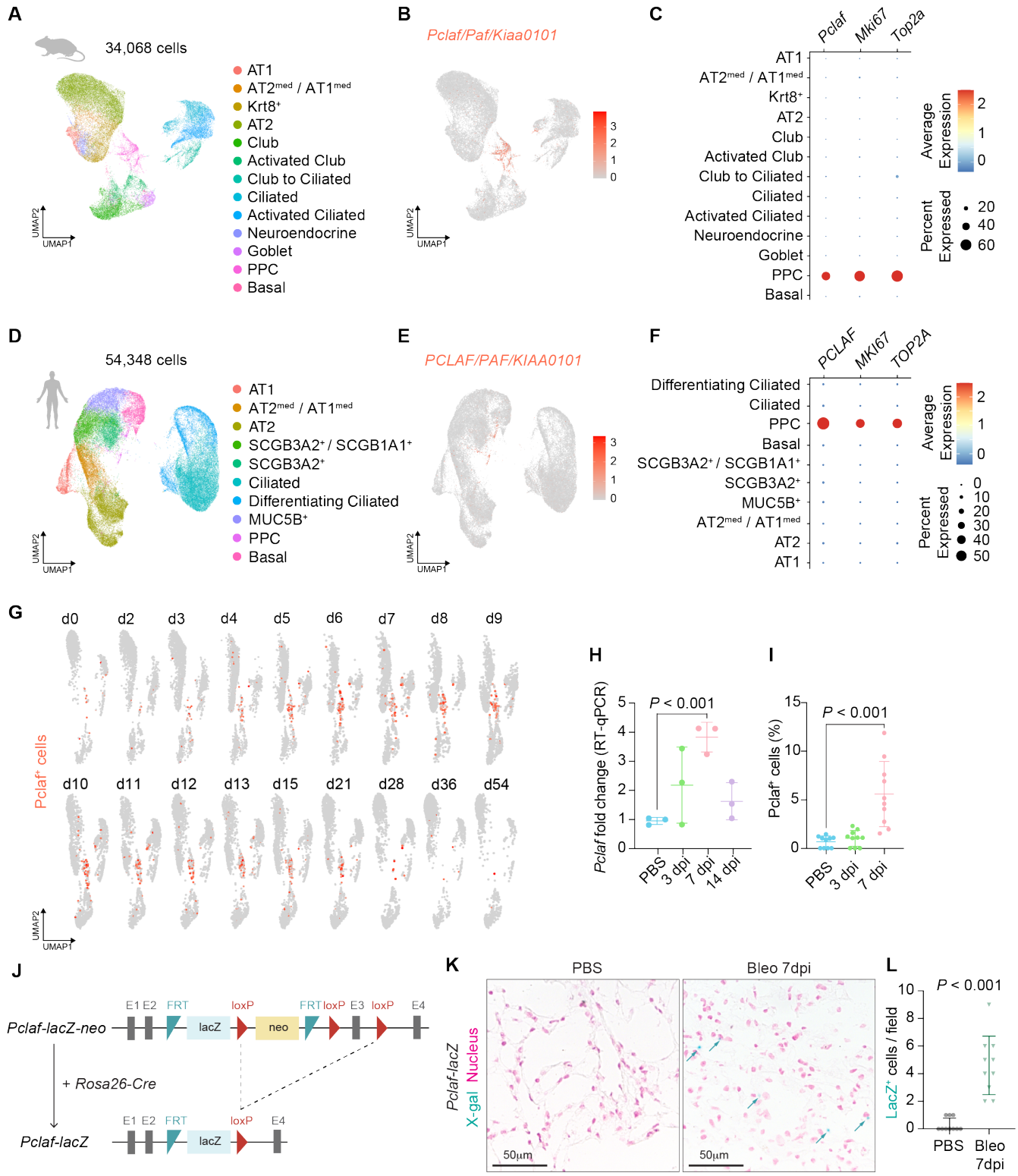

Fig. 1. Pclaf^{+} cells are elevated during lung regeneration.
(**A** to **C**) A public scRNA-seq data set (GSE141259) was generated by subjecting sorted cells from the mouse lung epithelial compartment at 18 different time points after bleomycin instillation. (**A**) Uniform manifold approximation and projection (UMAP)-embedding displays cells colored by cell type identity. (**B**) Feature plot of *Pclaf* expression. (**C**) Dot plots showing *Pclaf*, *Mki67*, and *Top2a* gene expression in each cell type. (**D** to **F**) A public scRNA-seq data set (GSE135893) was generated from the human lung cells of 20 pulmonary fibrotic diseases and 10 control lungs. (**D**) UMAP embedding displays cells colored by cell type identity. (**E**) Feature plot

of expression of *PCLAF*. (**F**) Dot plots for *PCLAF*, *MKI67*, and *TOP2A* gene expression in each cell type. (**G**) Feature plots of *Pclaf* expression in mouse lung at the indicated time points using data shown in Fig 1A. (**H** and **I**) Mouse lungs (n = 3) were collected after bleomycin (1.4 U/kg) had been added to the trachea at the indicated time points. (**H**) RT-qPCR analysis of the *Pclaf* mRNA level. Hprt was used as an internal control. (**I**) Quantification of $Pclaf^+$ cells by immunostaining. (**J**) Scheme of establishing *Pclaf-lacZ* knock-in mice. The neo cassette was deleted by breeding *Pclaf-lacZ-neo* with Rosa26-Cre driver. (**K**) Representative images of X-gal staining. *Pclaf-lacZ* mice were instilled with bleomycin (1.4 U/kg) or PBS (0 dpi). After 7 dpi, lungs were collected and stained for X-gal (5-bromo-4-chloro-3-indolyl-β-D-galactopyranoside; blue) and nuclear fast red (pink). (**L**) Quantification of $lacZ^+$ cells. Two-tailed Student's *t*-test; error bars: standard deviation (SD). The represented data are shown (n>=3).

Fig. 2

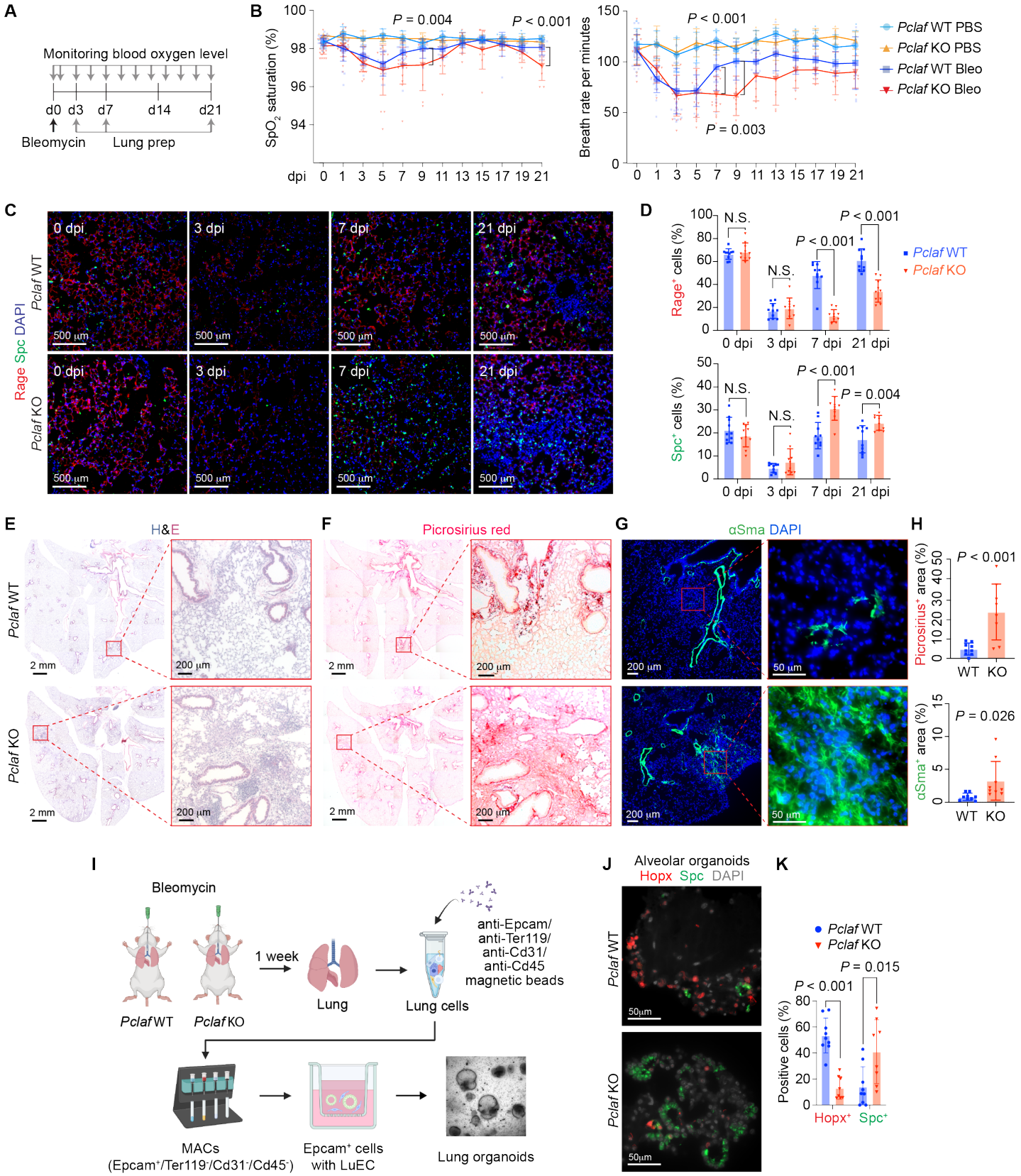

Fig. 2. *Pclaf* KO impairs lung regeneration.

(**A**) Experimental scheme for the bleomycin-induced lung injury model. *Pclaf* WT and KO mice were treated with phosphate-buffered saline (PBS) (n = 5 for *Pclaf* WT, n = 5 for *Pclaf* KO) or bleomycin (1.4 U/kg; n = 25

for *Pclaf* WT, n = 24 for *Pclaf* KO) by intratracheal instillation. The blood oxygen level (SpO_2) and breath rate were measured by pulse-oximetry at the indicated time points. At 3 days after injury (dpi, n = 7 for each group with bleomycin), 7 dpi (n = 8 for each group with bleomycin), and 21 dpi (n = 10 for *Pclaf* WT, n = 8 for *Pclaf* KO with bleomycin, n = 5 for each group with PBS (0 dpi)), the lungs were collected for further analysis. (**B**) The dynamics of SpO_2 levels (*left* panel) and breath rate per minute (*right* panel) were measured at the indicated time points. (**C** and **D**) Representative images (**C**) and quantification graph (**D**) of immunostaining for Rage (red; AT1) and Spc (green; AT2) at the indicated time points. (**E**) Representative images of hematoxylin and eosin (H&E) staining at 21 dpi. (**F**) Representative images of picrosirius staining (collagen fiber) at 21 dpi. (**G**) Representative images of immune-staining for alpha-smooth muscle actin (αSMA/Acta2; smooth muscle cell) at 21 dpi. (**H**) Quantification graphs of the picrosirius$^+$ area (*upper* panel) and αSMA$^+$ area (*bottom* panel). (**I** to **K**) The lung epithelial cells were isolated from bleomycin-treated lungs of *Pclaf* WT or *Pclaf* KO mice at 7 dpi by magnetic-activated cell sorting (MACS). The lung epithelial cells (Ter119$^-$/Cd31$^-$/Cd45$^-$/Epcam$^+$) were cultured with lung endothelial cells (Cd31$^+$) at a liquid-air interface to generate LOs. (**I**) Scheme of LO culture. (**J**) Images of alveolar type organoids fluorescently immunostained for Hopx (red; AT1) and Spc (green; AT2). (**K**) Quantification graph of Hopx$^+$ and Spc$^+$ cells. Two-tailed Student's *t*-test; error bars: SD. The represented images are shown (n>=3).

Fig. 3

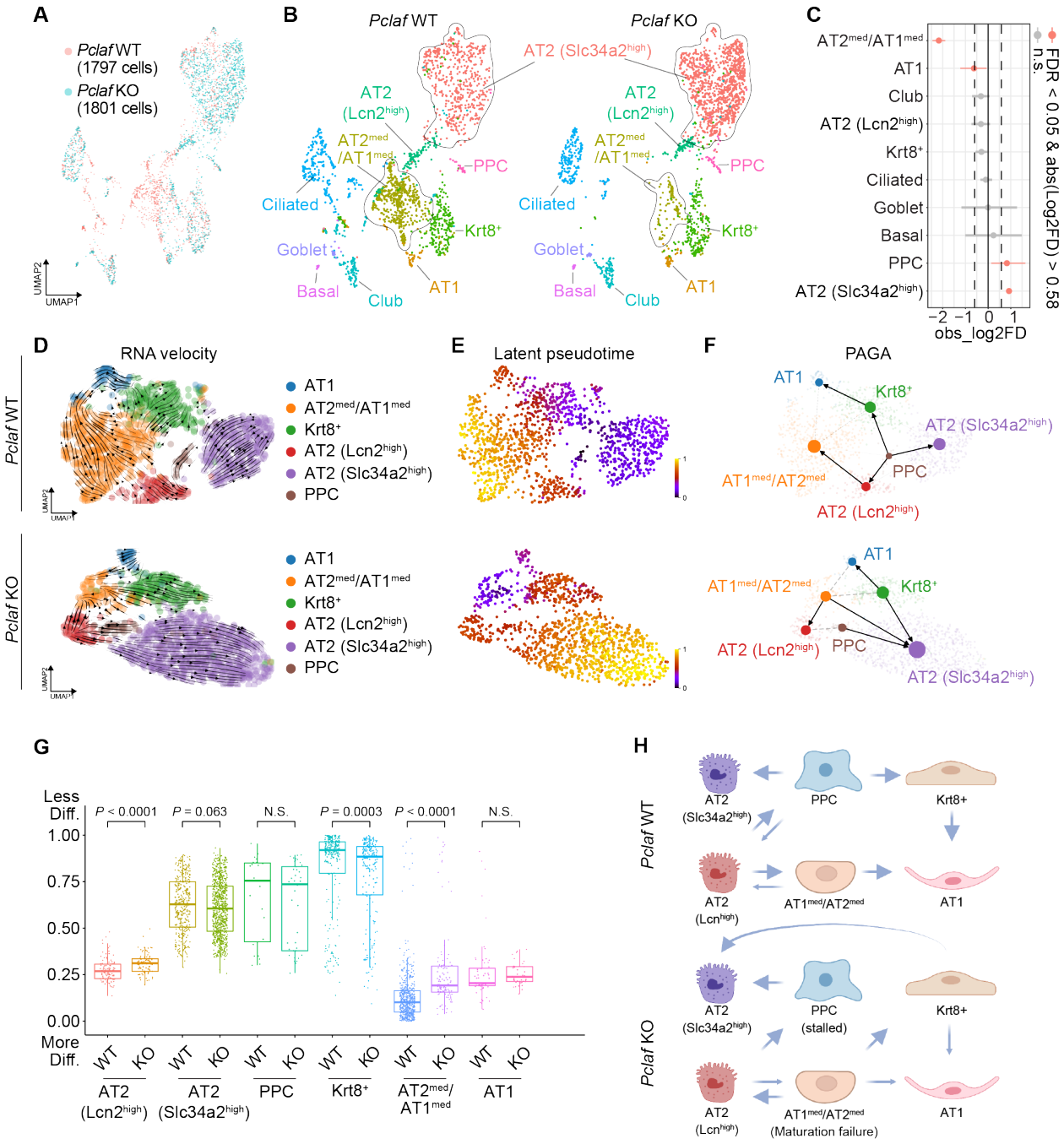

Fig. 3. *Pclaf* KO suppresses AT2 cell lineage plasticity.
(**A**) Integrated UMAP displaying each cell cluster of pulmonary epithelial cells isolated from *Pclaf* WT and KO mice. (**B**) UMAPs (split by *Pclaf* WT and KO) displaying each cell cluster, colored by cell types. (**C**) Cell proportion analysis of *Pclaf* WT vs. KO by cell type. (**D** to **F**) RNA velocity analyses (**D**), latent pseudotime analysis (**E**), and PAGA analysis (**F**) of *Pclaf* WT (*upper* panels) or KO (*bottom* panels) based on scRNA-seq are depicted. (**G**) Boxplots of predicted cluster-differentiation based on the CytoTRACE analysis. (**H**) Illustration of cellular trajectories in *Pclaf* WT (*upper* panel) or KO (*bottom* panel) cells during lung regeneration.

Fig. 4

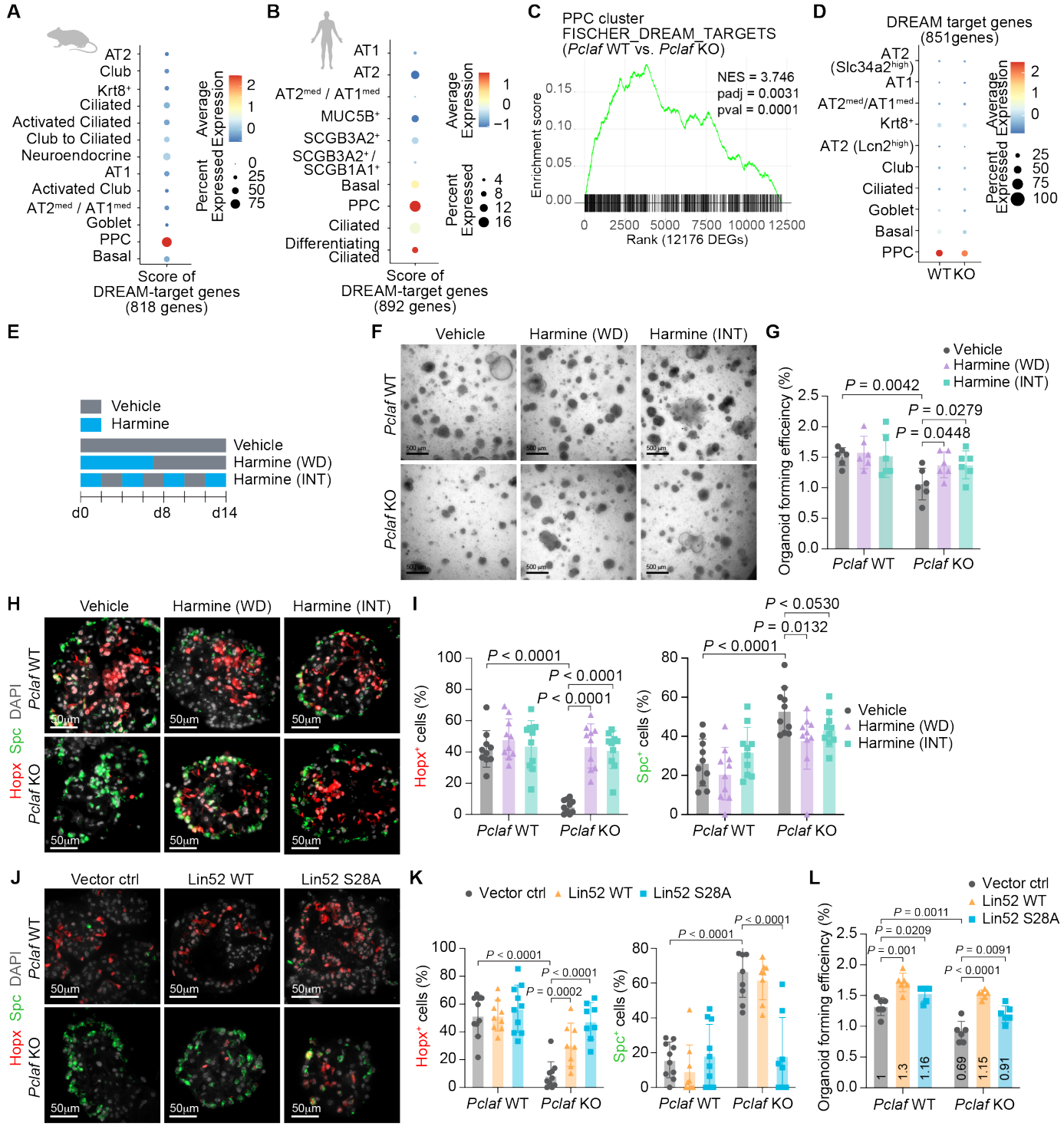

Fig. 4. PCLAF-DREAM axis mediates AT2 cell lineage plasticity for lung regeneration.
(**A**) Dot plots depicting transcriptional module scores of the gene sets of DREAM-target genes with the mouse scRNA-seq dataset shown in Fig. 1A. (**B**) Dot plots depicting transcriptional module scores of the gene sets of DREAM-target genes with the human scRNA-seq data set shown in Fig. 1D. (**C**) Gene set enrichment analysis (GSEA) of *Pclaf* WT vs. *Pclaf* KO in the PPC cluster using the data set shown in Fig. 3. The enrichment plot presents the gene sets of DREAM-target genes. (**D**) Dot plots depicting transcriptional module scores of the DREAM-target gene set using the data set shown in Figure 2. (**E**) Experimental scheme for LO culture under

stimuli of harmine (200 nM). Harmine was used to treat LOs for the first 7 days and withdrawn (WD). Alternatively, LOs were cultured with harmine intermittently (INT) at the indicated time points. (**F**) The representative bright-field z-stack images of LOs on day 12. (**G**) Quantification graph of lung OFE. (**H**) Representative images of IF staining for Hopx (AT1; red) and Spc (AT2; green) on day 14. (**I**) Quantification graph of $Hopx^+$ and Spc^+ cells. (**J** to **L**) Isolated lung epithelial cells were transduced with RFP, Lin52 WT, or Lin52 S28A by lentivirus and then cultured with LO. (**J**) Representative images of IF staining for Hopx (AT1; red) and Spc (AT2; green) on day 14. (**K**) Quantification graph of $Hopx^+$ and Spc^+ cells. (**L**) Quantification graph of lung OFE. Two-tailed Student's *t*-test; error bars: SD. The represented images and data are shown (n>=3).

Fig. 5

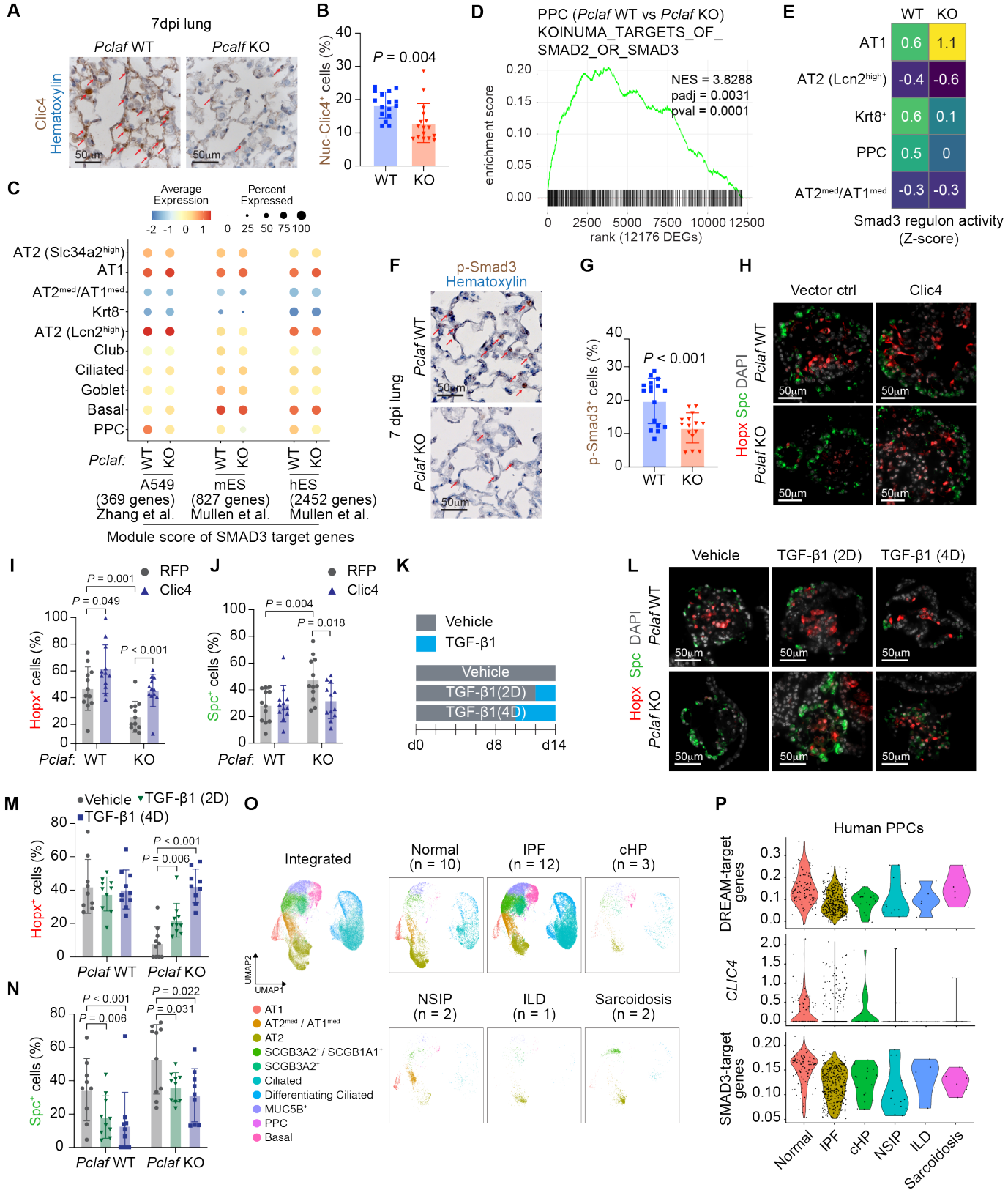

Fig. 5. PCLAF-DREAM-mediated CLIC4-TGF-β signaling axis is required for AT1 cell differentiation. (**A**) Representative images of *Pclaf* WT and *Pclaf* KO lung at 7 dpi, chemically immunostained for Clic4. (**B**) Quantification graph of nucleus Clic4^{+} cells. (**C**) Dot plots depicting transcriptional module scores of SMAD3 gene sets from A549, mouse embryonic stem cells (mES), and human embryonic stem cells (hES) using the

scRNA-seq dataset shown in Fig. 3. (**D**) GSEA of *Pclaf* WT vs. *Pclaf* KO in the PPC cluster using the data set shown in Fig. 3. The enrichment plot presents the gene sets of SMAD2 or SMAD3 target genes. (**E**) Z-score of Smad3 regulon activity by cell type and genome, analyzed by pySCENIC using the data set shown in Fig. 3. (**F**) Representative images of *Pclaf* WT and *Pclaf* KO lung at 7 dpi, chemically immunostained for p-Smad3. (**G**) Quantification graph of p-Smad3$^+$ cells. (**H** to **J**) Isolated lung epithelial cells were transduced with RFP- or CLIC4-expressing lentiviruses and cultured with LO. (**H**) Representative images of IF staining for Hopx (AT1; red) and Spc (AT2; green) on day 14. (**I** and **J**) Quantification of Hopx$^+$ (**I**) and Spc$^+$ cells (**J**). (**K** to **N**) *Pclaf* WT, or KO lung epithelial cells-derived LOs were cultured with TGF-β1 (2 ng/ml) for 2 days (TGFβ1 [2D]) or 4 days (TGFβ1 [4D]). (**K**) Experimental scheme for TGF-β1 treatment. **l**, Representative images of IF staining for Hopx (AT1; red) and Spc (AT2; green) on day 14. (**M** to **N**) Quantification of Hopx$^+$ (**M**) and Spc$^+$ cells (**N**). (**O**) UMAP plots displaying each cell cluster from the scRNA-seq datasets of normal human lung and fibrotic diseases shown in Fig. 1D. (IPF; idiopathic pulmonary fibrosis, cHP; chronic hypersensitivity pneumonitis, NSIP; nonspecific interstitial pneumonia, ILD; interstitial lung disease). (**P**) Violin plots showing the expression of module scores of DREAM-target genes, *CLIC4* expression, and hES-SMAD3-target genes in the PPC clusters from the human scRNA-seq data set. Two-tailed Student's *t*-test; error bars: SD. The represented images are shown (n>=3).

Fig. 6

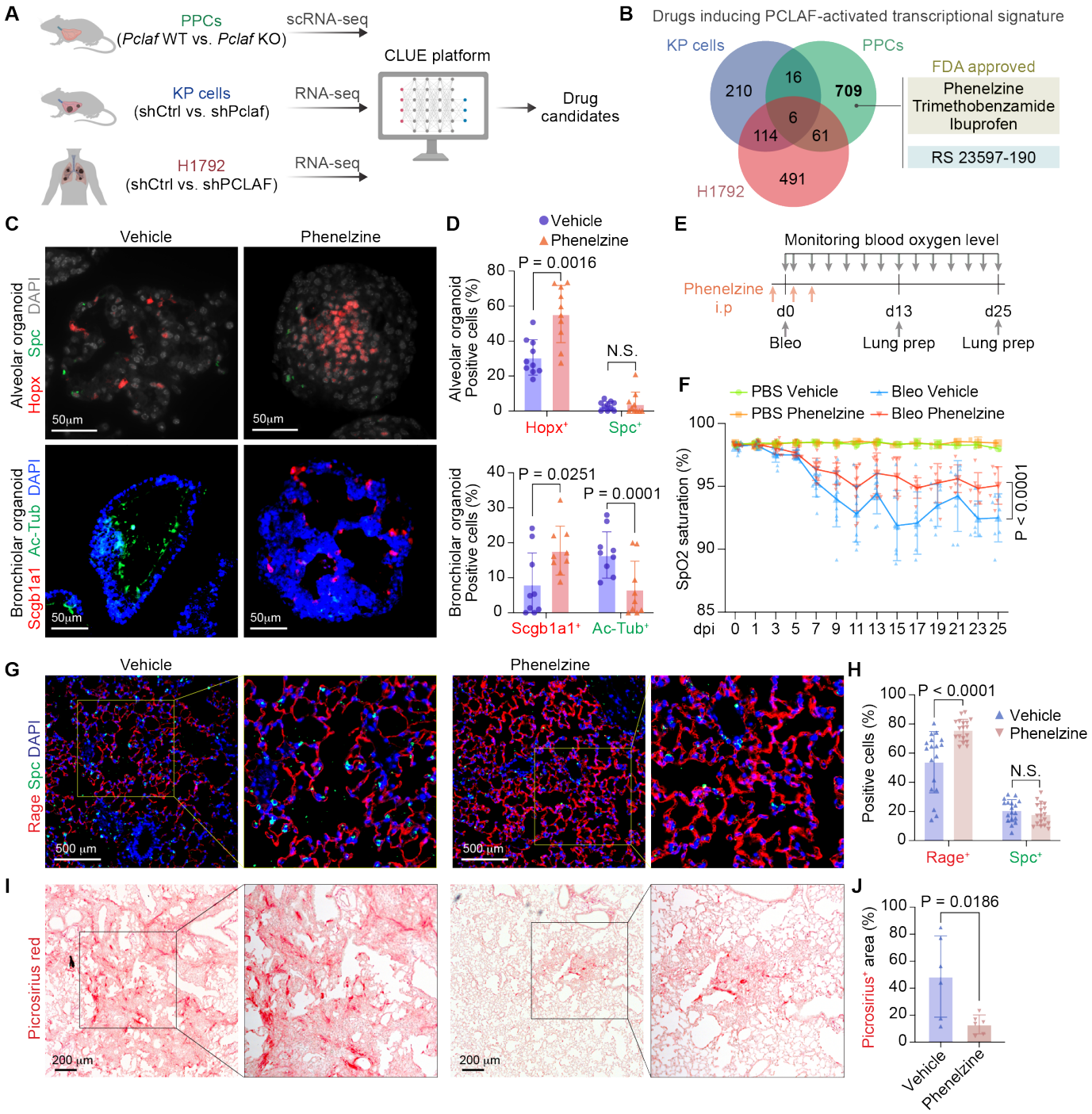

Fig. 6. Pharmacological mimicking of PCLAF-DREAM-activated transcriptional signature restores lung regeneration.

(**A**) Experimental scheme to identify drug candidates by the CLUE platform. (**B**) Venn diagram of Connectivity Map results, identifying drug candidates specific to normal lung PPCs. (**C**) Representative images of LOs with phenelzine (10 μM) that fluorescently immunostained for Hopx (AT1; red; *upper* panels), Spc (AT2; green; *upper* panels), Scgb1a1 (Club; red; *bottom* panels), and Ac-Tub (Ciliated; green; *bottom* panels). (**D**) Quantification graph of Hopx$^+$ (*upper* panel), Spc$^+$ (*upper* panel), Scgb1a1$^+$ (*bottom* panel), and Ac-Tub$^+$ (*bottom* panel) cells. (**E**) Experimental scheme for bleomycin-induced lung regeneration by phenelzine. Mice were treated with bleomycin (2.8 U/kg) by intratracheal instillation. The vehicle control (DMSO, n = 10) or phenelzine (n = 10; 750 μg/head) were administered by intraperitoneal injection at -1, 1, and 3 dpi. The blood oxygen level (SpO_2)

and breath rate were measured by pulse oximetry every other day. At 13 dpi (n = 4 for each group) and 25 dpi (n = 6 for each group), lungs were collected for further analysis. (**F**) The dynamics of spO_2 levels were measured at the indicated time points. Two-way ANOVA with post-hoc Tukey test. (**G**) Representative images of the lungs at 13 dpi, fluorescently immunostained for Rage (AT1; red) and Spc (AT2; green). (**H**) Quantification graph of $Rage^+$ or Spc^+ cells. (**I**) Representative images of picrosirius staining at 25 dpi. (**J**) Quantification graphs of the $picrosirius^+$ area. Two-tailed Student's *t*-test except for Figure 5f; error bars: SD. The representative images are shown (n>=3).

Fig. S1

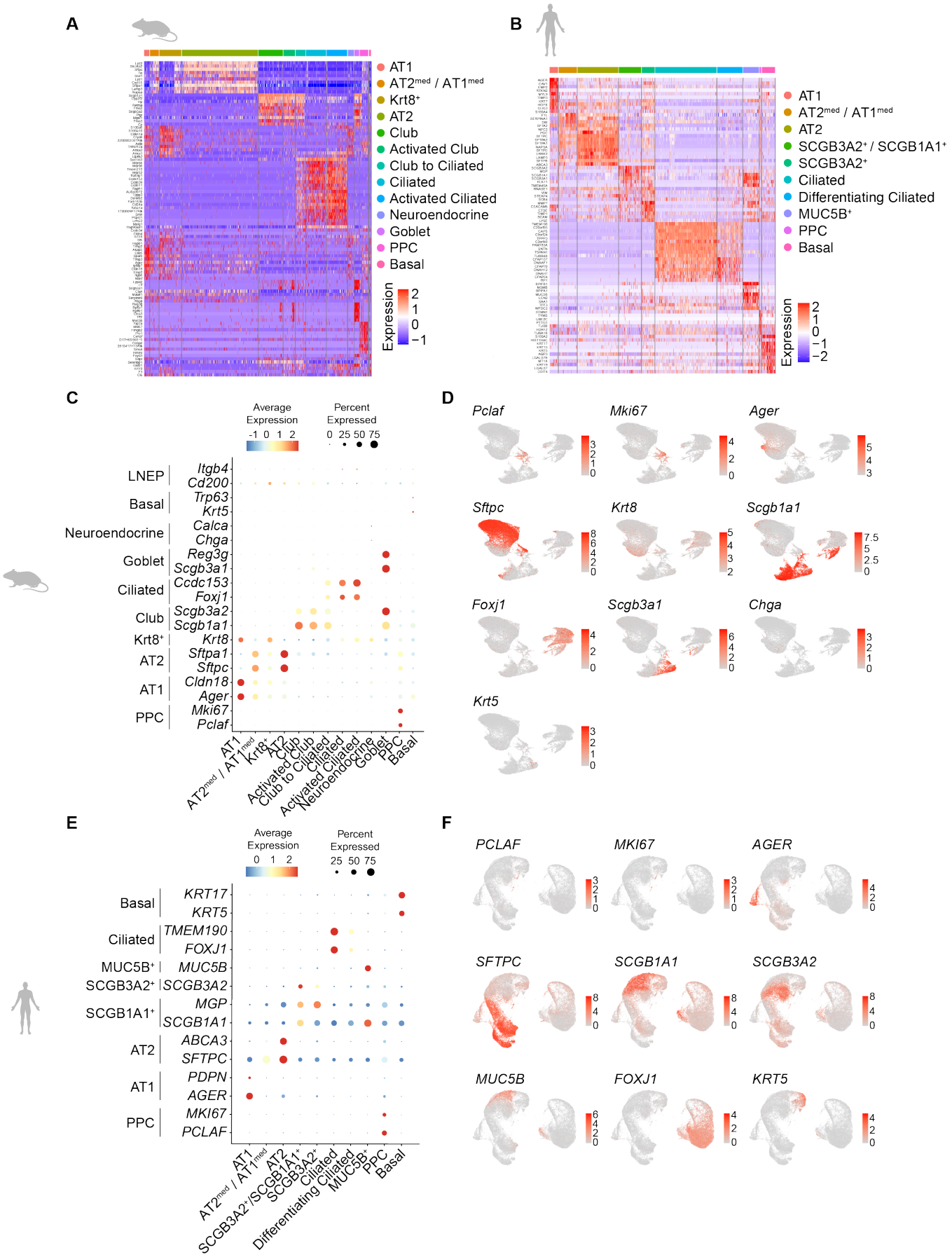

Fig. S1. The cell type annotation of human and mouse lung single-cell transcriptomics.

(**A**) Heatmap of gene expression of the top 10 genes in each cell type of mouse lung using data shown in Fig. 1A. (**B**) Heatmap of gene expression of the top 10 genes in each cell type of human lung using data shown in Fig. 1D. (**C**) Dot plots for mouse lung epithelial marker gene expression in each cell type. (**D**) Feature plots of mouse lung epithelial marker gene expression. (**E**) Dot plots for human lung epithelial marker gene expression in each cell type. (**F**) Feature plots of human lung epithelial marker gene expression.

Fig. S2

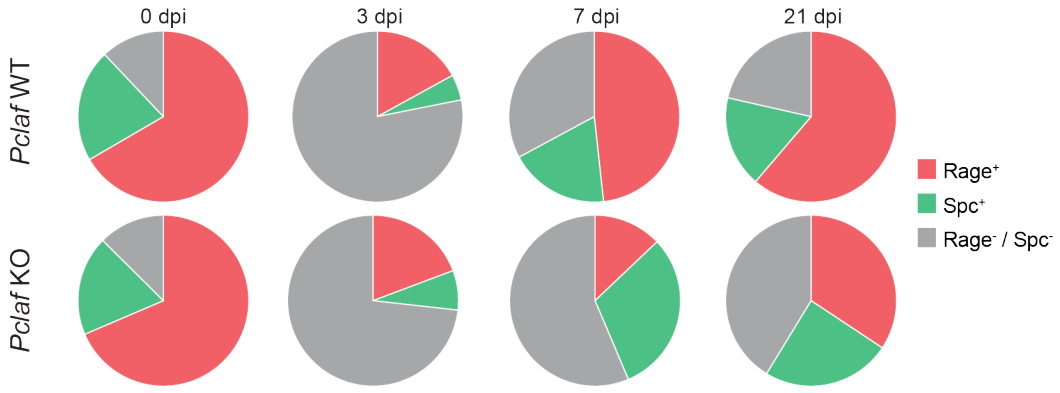

Fig. S2. *Pclaf* KO inhibits AT1 regeneration and promotes AT2 repopulation.
Pie plots of Rage$^+$ (AT1) and Spc$^+$ (AT2) cells using data shown in Fig. 1C.

Fig. S3

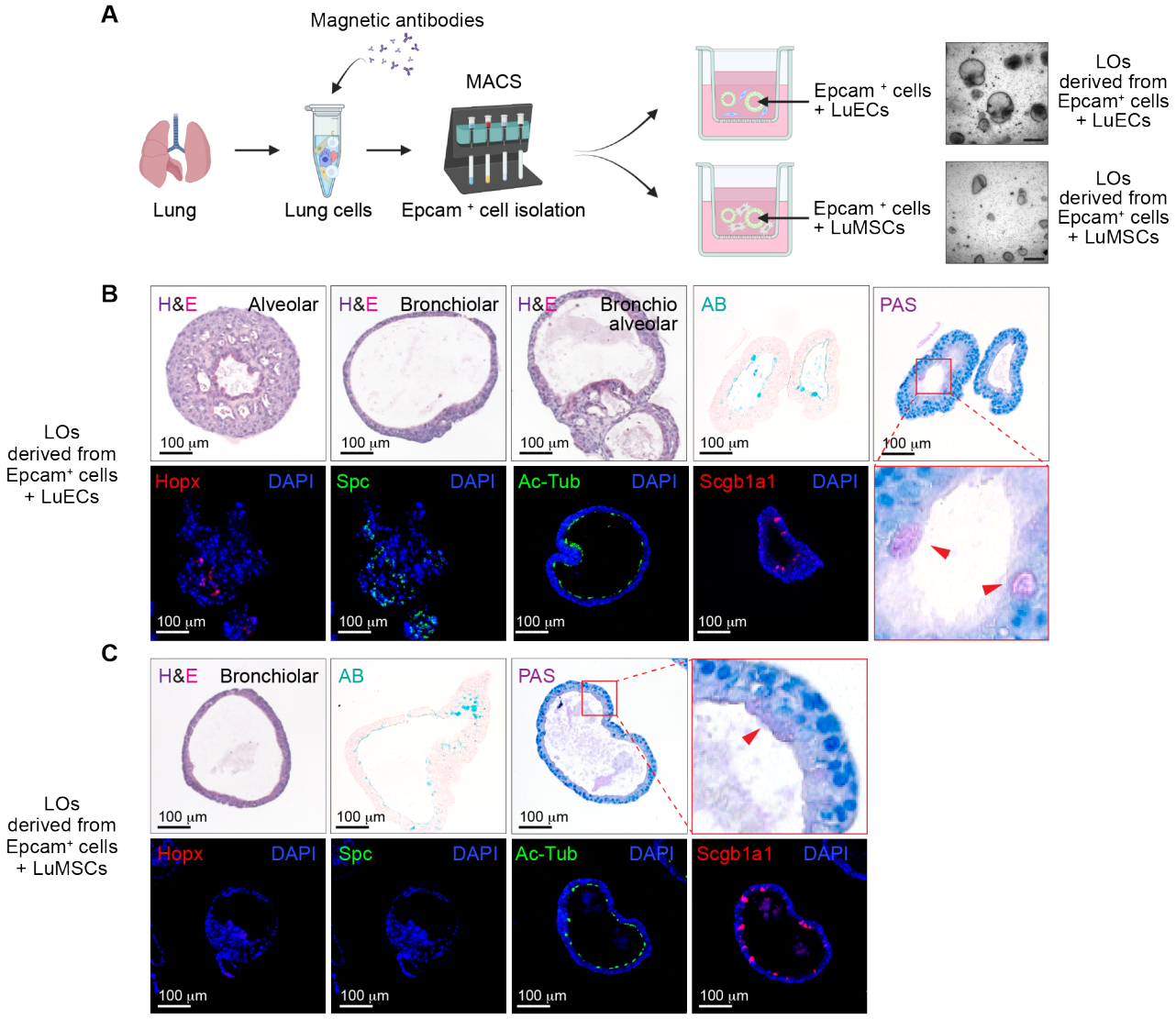

	Hopx (AT1)	Spc (AT2)	Scgb1a1 (Club)	Ac-Tub (Ciliated)	AB (Goblet)	PAS (Goblet)
LOs on LuECs	+	+	+	+	+	+
LOs on LuMSCs	n.d.	n.d.	+	+	+	+

Fig. S3. Comparison of LO culture systems.
(**A**) Scheme of LO culture. The lung epithelial cells were isolated from WT mice by MACS and cultured with LuECs or LuMSCs at a liquid-air interface to grow LOs. (**B** and **C**) Representative images of organoids for hematoxylin and eosin (H&E), alcian blue (AB), and periodic acid-Schiff (PAS) staining (*upper* panels), and immunostained for Hopx (AT1), Spc (AT2), Ac-Tub (Ciliated), and Scgb1a1 (Club; *bottom* panels) of organoids with LuECs (**B**) and with LuMSCs (**C**). (**D**) Table of positive cells using data shown in Fig S3B and C. The represented images are shown (n>=3).

Fig. S4

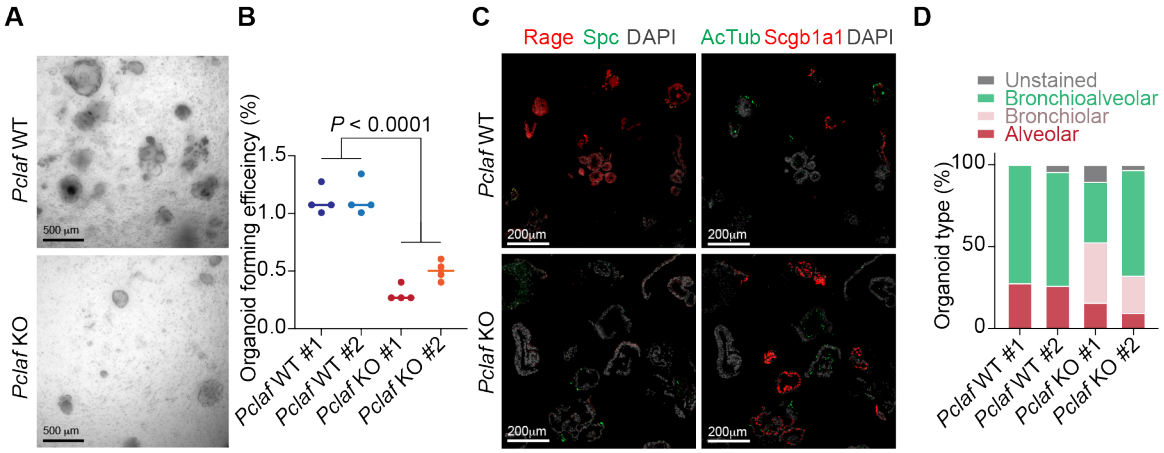

Fig. S4. *Pclaf* KO inhibits alveolar-type lung organoid formation.
(**A** to **D**), The lung epithelial cells were isolated from bleomycin-treated lungs of *Pclaf* WT or *Pclaf* KO mice at 7 dpi (bleomycin administration) by magnetic-activated cell sorting (MACS). The lung epithelial cells ($Ter119^-$/$Cd31^-$/$Cd45^-$/$Epcam^+$) were cultured with lung endothelial cells ($Cd31^+$) at a liquid-air interface to generate LOs. (**A**) Bright-field z-stack images of LOs at day 12. (**B**) Quantification graph of lung OFE. (**C**) Representative images of LOs that were fluorescently immunostained for Rage (AT1; red; *left* panels), Spc (AT2; green; *left* panels), acetyl-Tubulin (Ciliated; AcTub; green; *right* panels), and Scgb1a1 (Club; red; *right* panels). (**D**) Quantification graph of organoid type. Two-tailed Student's *t*-test; error bars: SD. The represented images and data are shown (n>=3).

Fig. S5

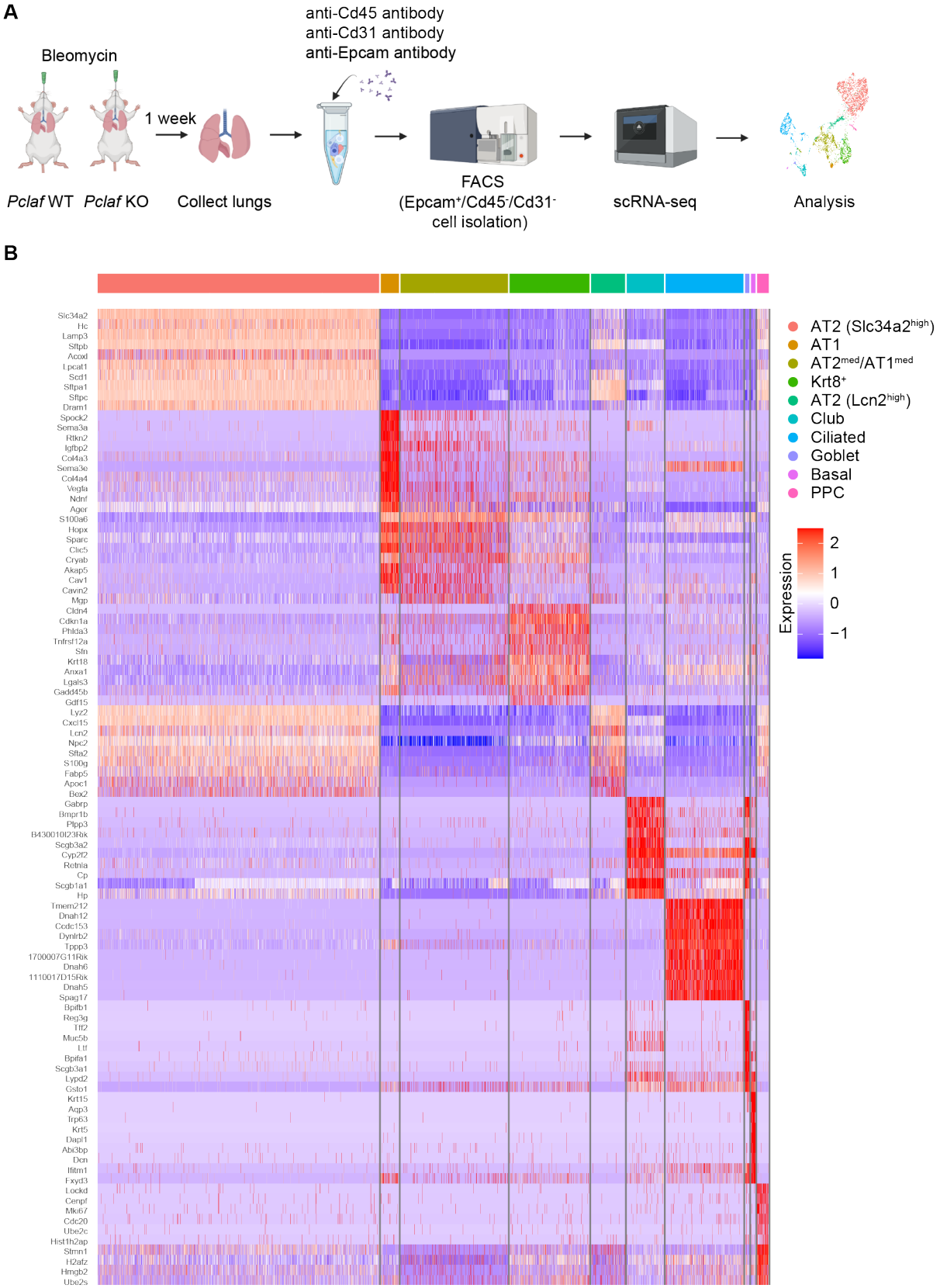

Fig. S5. Scheme of single-cell transcriptomics of *Pclaf* WT and KO mouse lung tissues.

(**A**) Scheme of scRNA-seq. Lung epithelial cells were isolated from *Pclaf* WT and KO mice (treated with bleomycin) by fluorescence-activated cell sorting (FACS). $CD31^-/CD45^-/Epcam^+$ cells were used to generate sequencing data using the 10X genomics single-cell sequencing service. (**B**) Heatmap of gene expression-based cell clusters of the top 10 genes in each cell type of mouse lung using data shown in Fig. 3B.

Fig. S6

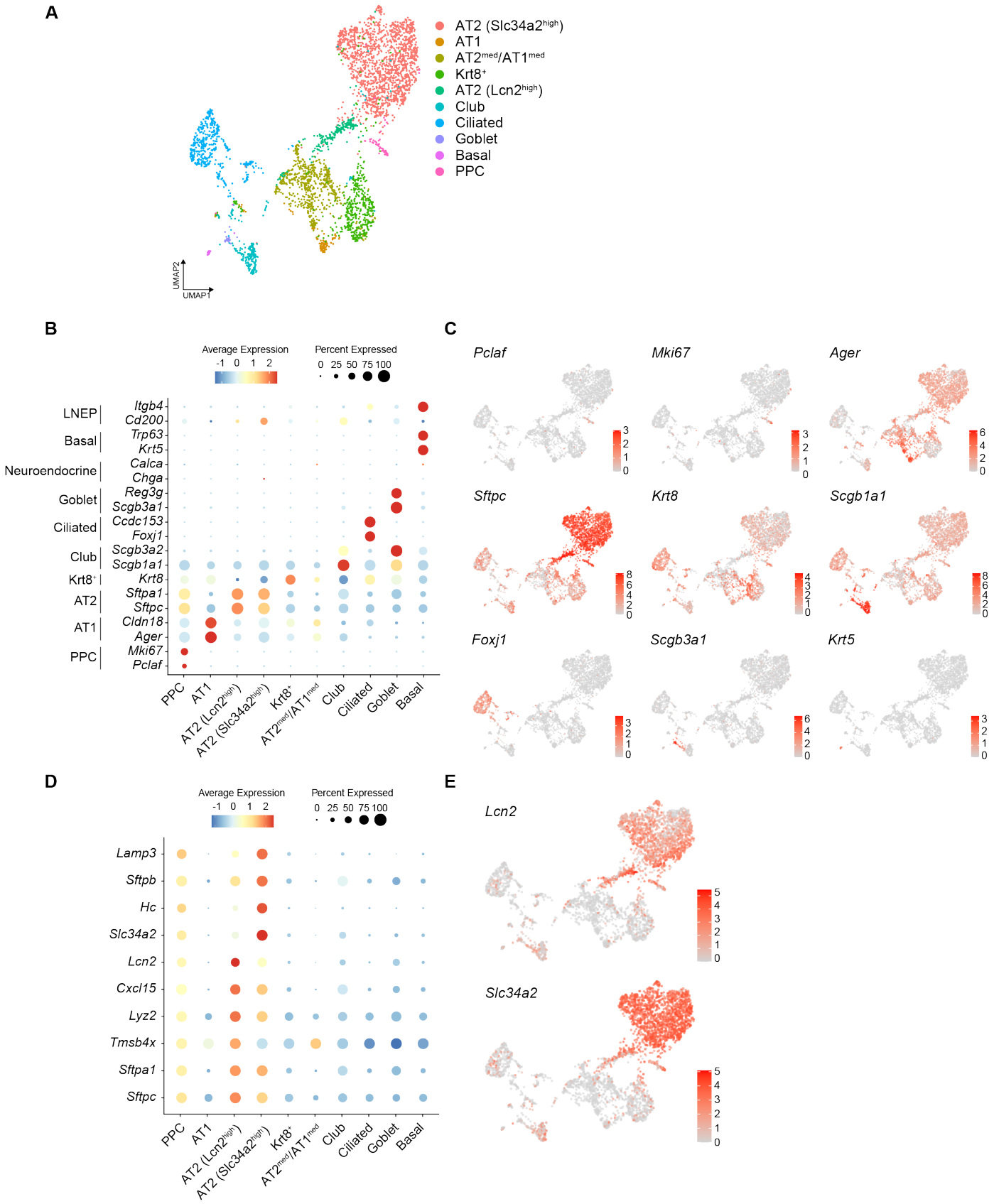

Fig. S6. Cell type annotation of mouse lung single-cell transcriptomics.
Analysis of the scRNA-seq dataset is shown in Fig. 3B. (**A**) UMAP displays each cell cluster, colored by cell type. (**B**) Dot plots for mouse lung epithelial marker gene expression quantification of each cell type. (**C**) Feature

plots of mouse lung epithelial marker gene expression. (**D**) Dot plots for genes specifically expressed in AT2(Lcn^{high}) and AT2(Slc34a^{high}). (**E**) Feature plots displaying the expression of *Lcn2* and *Slc34a2*.

Fig. S7

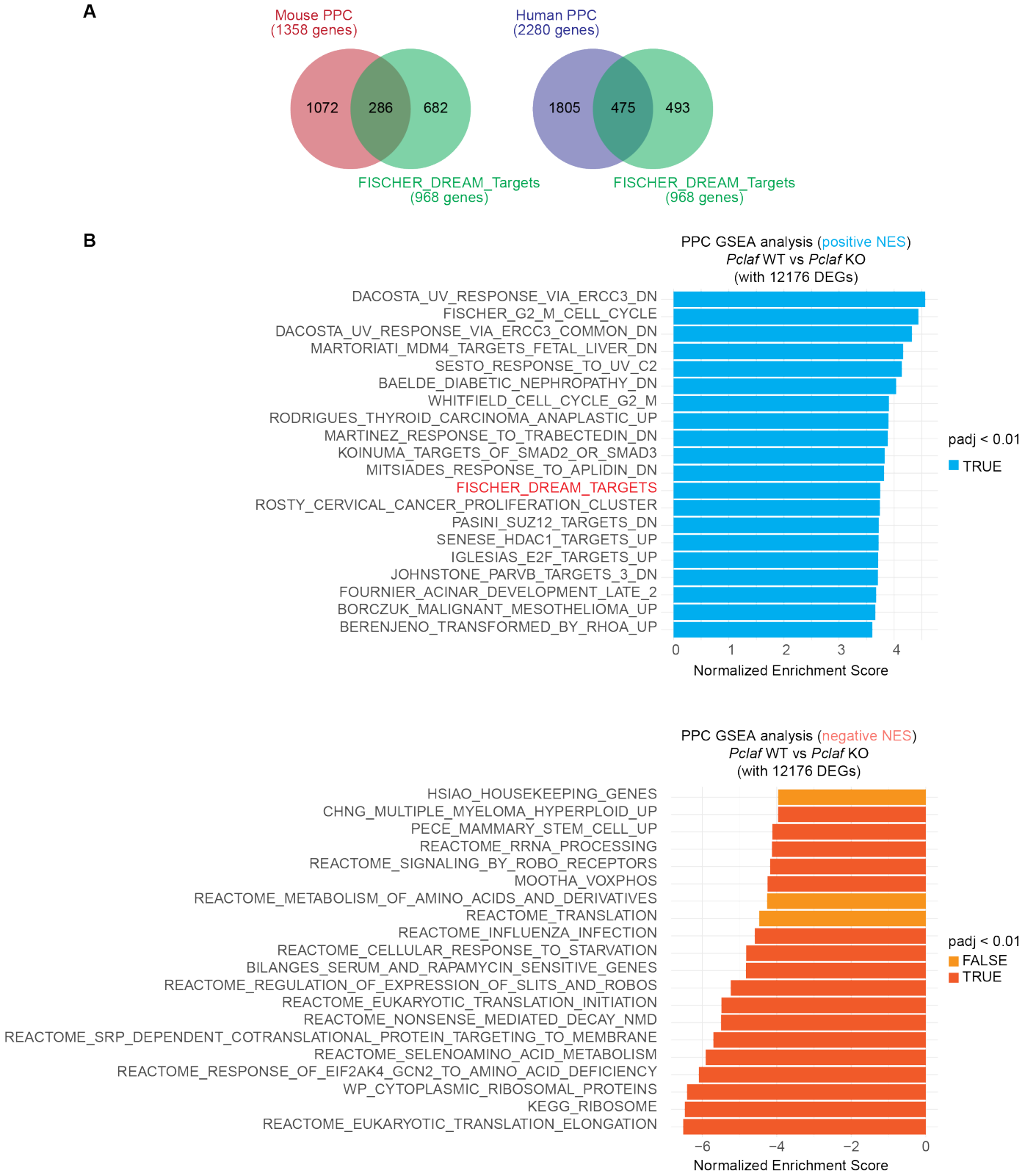

Fig. S7. *Pclaf* KO downregulates DREAM-target gene expression in PPC.
(**A**) Venn diagram analysis of DREAM target genes vs. genes specifically expressed in the PPC clusters (mouse scRNA-seq dataset shown in Fig. 1A or the human scRNA-seq dataset shown in Fig. 1D). (**B**) Top 20 gene sets (*upper* panel) and bottom 20 gene sets (*bottom* panel) of GSEA with 12,176 DEGs between *Pclaf* WT PPCs and *Pclaf* KO PPCs.

Fig. S8

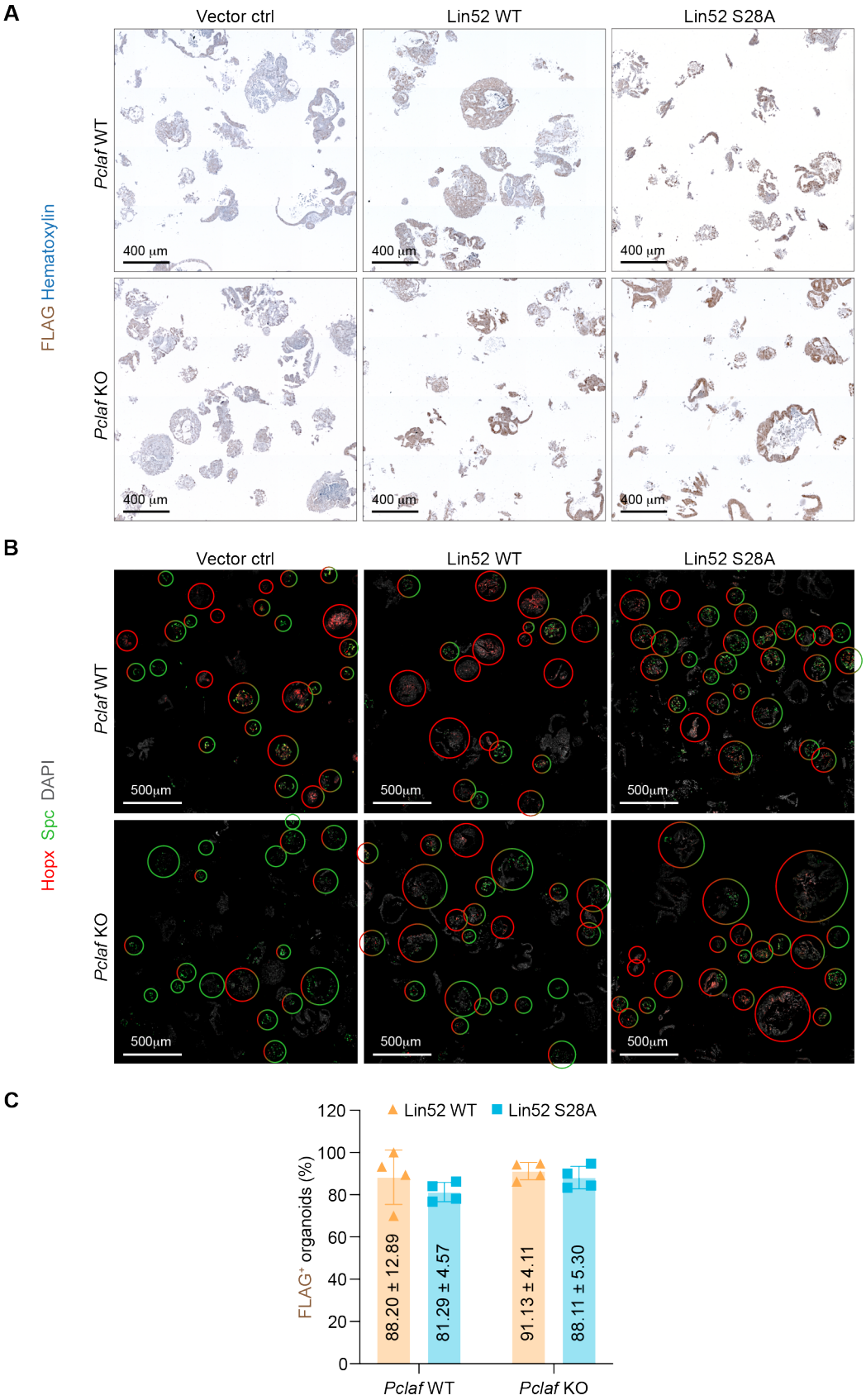

Fig. S8. Transduction efficiency of lentiviruses encoding Lin52-WT or Lin52 S28A in LOs.

Isolated lung epithelial cells were transduced with RFP, Lin52 WT, or Lin52 S28A by lentivirus and then cultured with LO. (**A**) Representative images chemically immunostained for FLAG. (**B**) Representative images of IF staining for Hopx (AT1; red) and Spc (AT2; green) on day 14. The circles (in red-green mixed) indicate the relative ratio of $Hopx^+$ to Spc^+ cells in LOs. (**C**) Quantification of $FLAG^+$ LOs. The represented images and data are shown (n>=3); error bars: SD.

Fig. S9

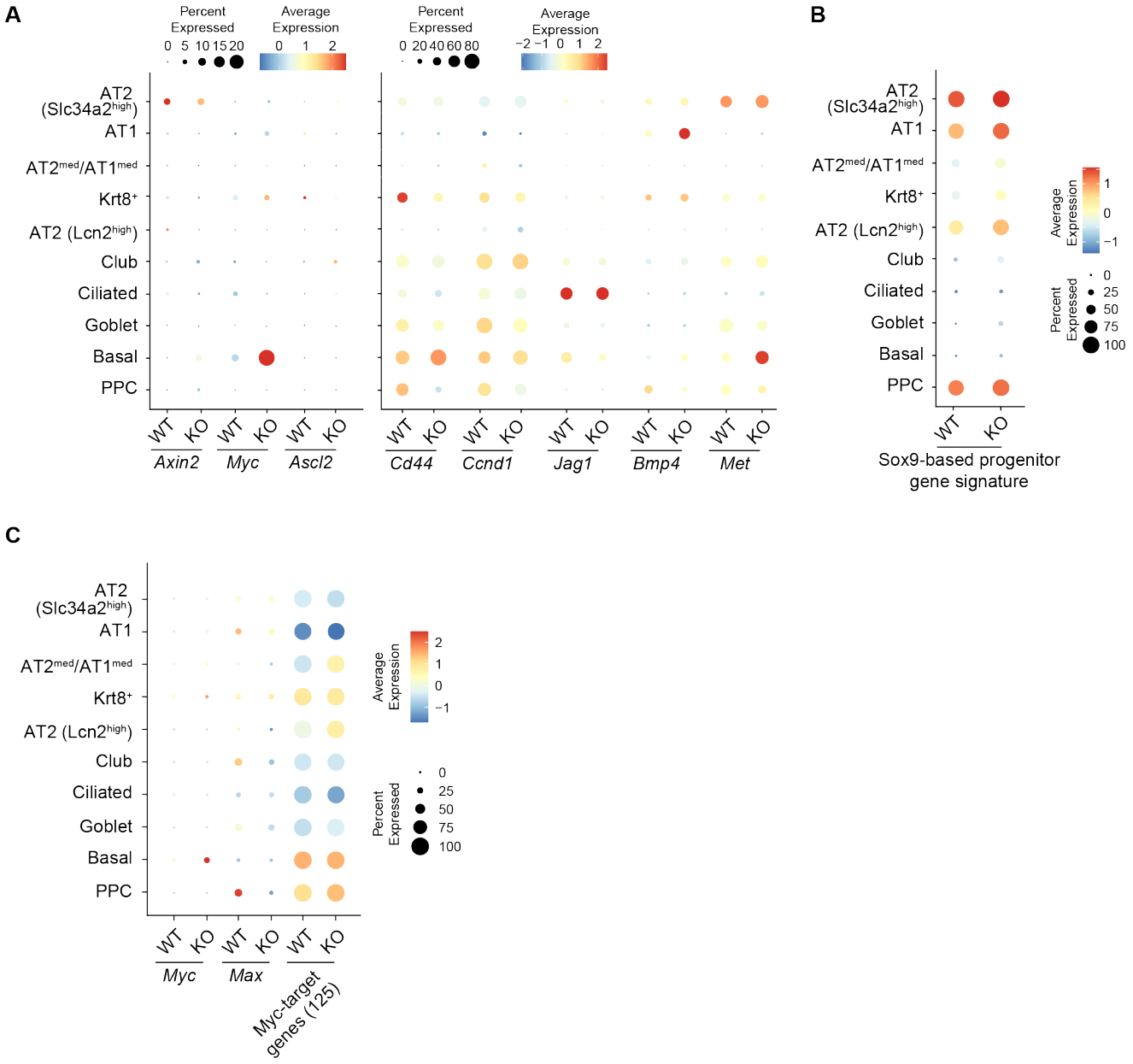

Fig. S9. Impact of *Pclaf* KO on Wnt signaling, Sox9, and Myc transcriptional signatures.
(**A** to **C**) Dot plots displaying each gene expression from the scRNA-seq dataset shown in Fig. 3. (**A**) Dot plots showing the expression of Wnt signaling target genes in each cell type. (**B**) Dot plots depicting transcriptional module scores of the Sox9-based progenitor cell signature gene set. (**C**) Dot plots showing the expression of *Myc* and *Max* and transcriptional module scores of the Myc-target gene set. Of note, *Pclaf* KO barely alters Wnt signaling and Sox9-based progenitor transcriptional signature.

Fig. S10

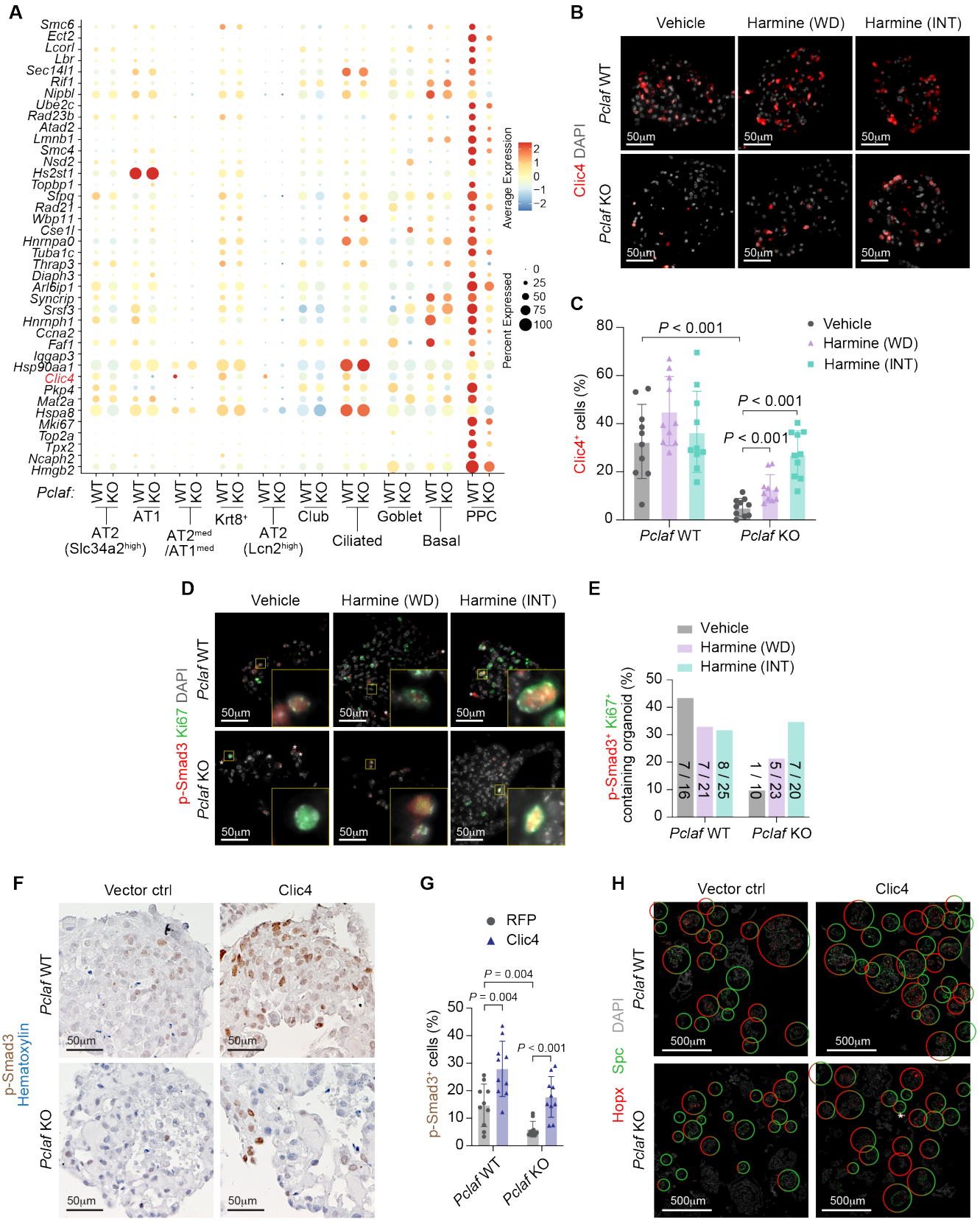

Fig. S10. Pharmacological or genetic activation of the DREAM axis rescues *Pclaf* KO-inhibited TGF-β signaling.

(**A**) Dot plots displaying the top 40 differently expressed DREAM target genes in each cell type. (**B** to **E**) LOs treated with harmine (shown in Fig. 3E) were immunostained with indicated antibodies. (**B**) Representative

images of IF staining for Clic4 (red). (**C**) Quantification of the Clic4$^+$ cells. (**D**) Representative images of IF staining for p-Smad3 (red) and Mki67 (green) on day 14. (**E**) Quantification of LOs containing p-Smad3 and Mki67 double-positive cells. (**F** to **J**) Isolated lung epithelial cells were transduced with RFP- or CLIC4-expressing lentiviruses and cultured with LO. (**F**) Representative images of *Pclaf* WT and *Pclaf* KO LOs at day 14, chemically immunostained for p-Smad3. (**G**) Quantification graph of p-Smad3$^+$ cells. (**H**) Images of IF staining for Hopx (AT1; red) and Spc (AT2; green) on day 14. The circle color indicates the relative ratio of Hopx$^+$ to Spc$^+$ cells. Two-tailed Student's *t*-test; error bars: SD. The representative images are shown (n>=3).

Fig. S11

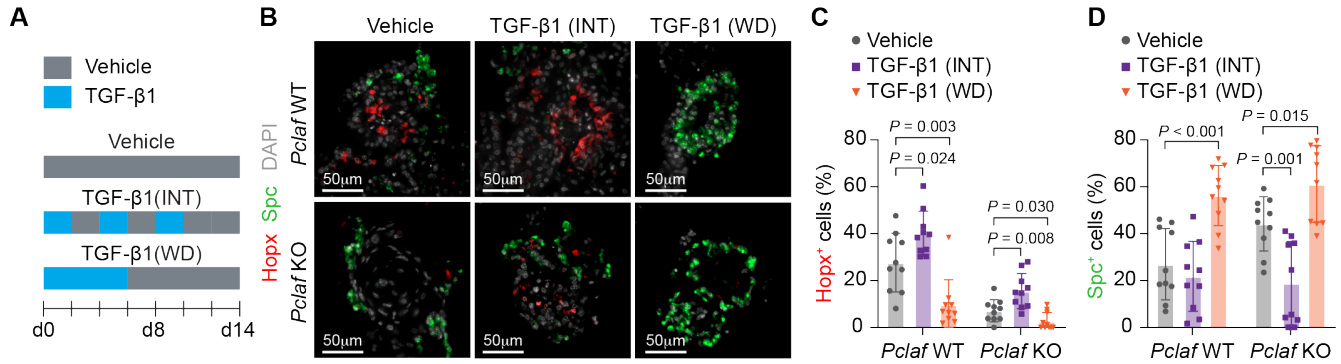

Fig. S11. TGF-β rescues *Pclaf* KO-impaired cell plasticity.
(**A** to **D**) Murine lung epithelial cells were cultured for LOs under stimuli of TGF-β1 (2 ng/ml). TGF-β1 was used to treat LOs for the first 6 days and withdrawn (WD). Alternatively, LOs were cultured with TGF-β1 intermittently (INT) at the indicated time points. (**A**) Experimental scheme for LO culture. (**B**) Representative images of IF staining for Hopx (AT1; red) and Spc (AT2; green) on day 14. (**C** and **D**) Quantification of Hopx$^+$ (**C**) and Spc$^+$ cells (**D**). Two-tailed Student's *t*-test; error bars: SD. The representative images are shown (n>=3). TGF-β1 (INT) rescued *Pclaf* KO-impaired alveolar cell plasticity (AT1 cell generation from AT2 cells). In contrast, TGF-β1 (WD) inhibited AT1 cell generation regardless of *Pclaf* WT and *Pclaf* KO. These data suggest that the temporal activity of TGF-β signaling is pivotal for AT2-to-AT1 cell transition.

Fig. S12

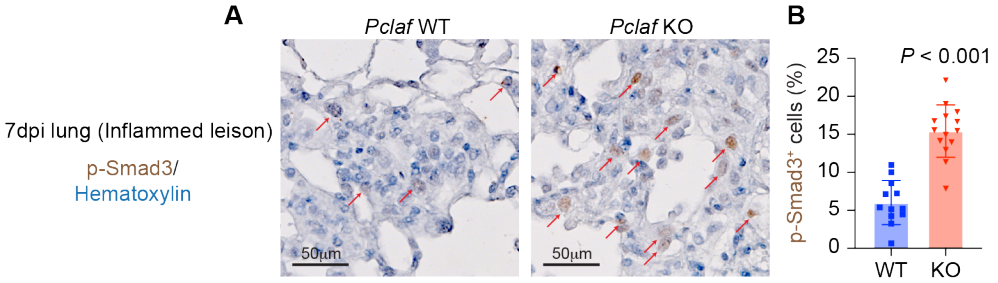

Fig. S12. Elevated TGF-β signaling in inflamed lesions by *Pclaf* KO.
(**A**) Images of immunostaining for p-Smad3 of the inflamed lesion from *Pclaf* WT and *Pclaf* KO lung tissues at 7 dpi. (**B**) Quantification graph of p-Smad3^{+} cells. Two-tailed Student's *t*-test; error bars: SD. The representative images are shown (n>=3).

Fig. S13

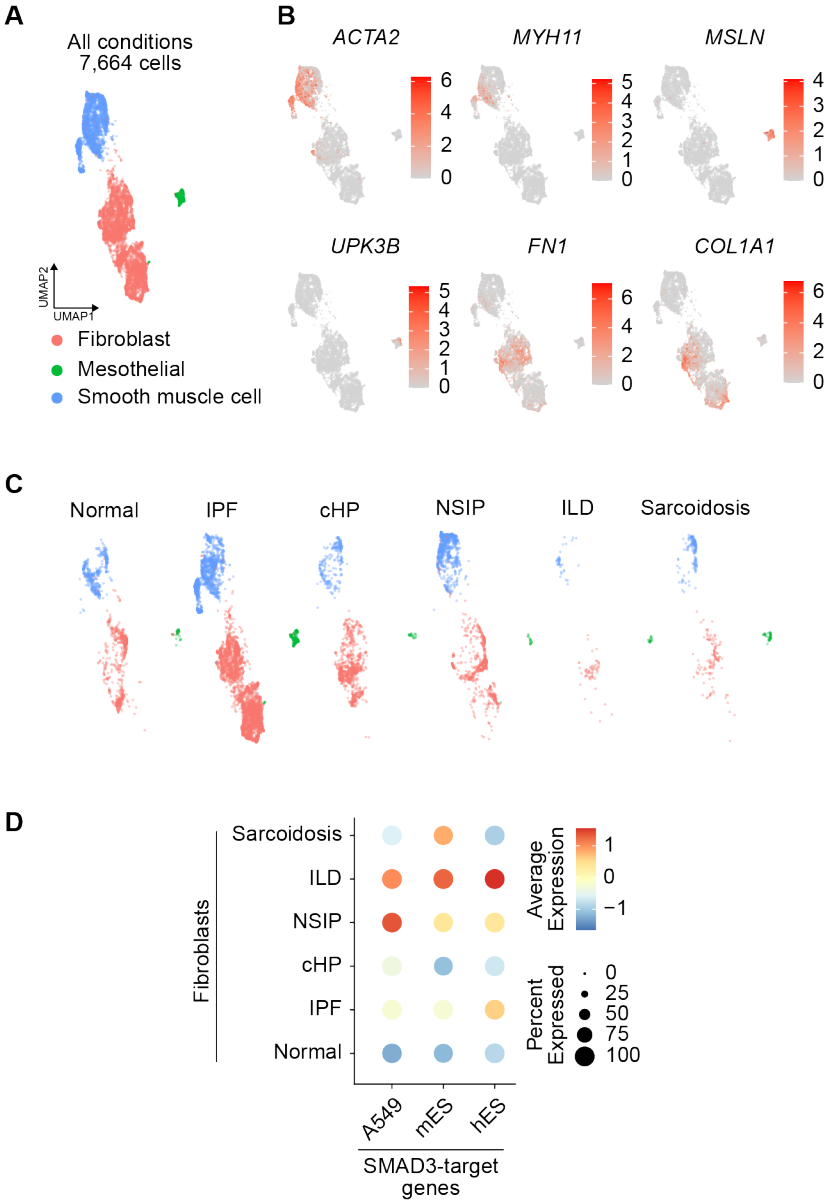

Fig. S13. Elevated TGF-β signaling in lung fibroblasts of IPF patients.
(**A**) UMAP showing the Mesenchymal compartment (*EPCAM*$^-$, *PTPRC*$^-$, and *PECAM*$^-$ cells) from the human scRNA-seq dataset (GSE135893; normal, IPF, cHP, NSIP, ILD, and Sarcoidosis). (**B**) Feature plots of indicated marker genes. *ACTA2* and *MYH11* for smooth muscle cells; *MSLN* and *UPK3B* for mesothelial cells; *FN1* and *COL1A1* for fibroblasts. (**C**) UMAP embedding displays cells colored by cell types split by each disease type. (**D**) Dot plots showing the expression of indicated genes and module scores of SMAD3-target gene sets in human lung fibroblasts.

Fig. S14

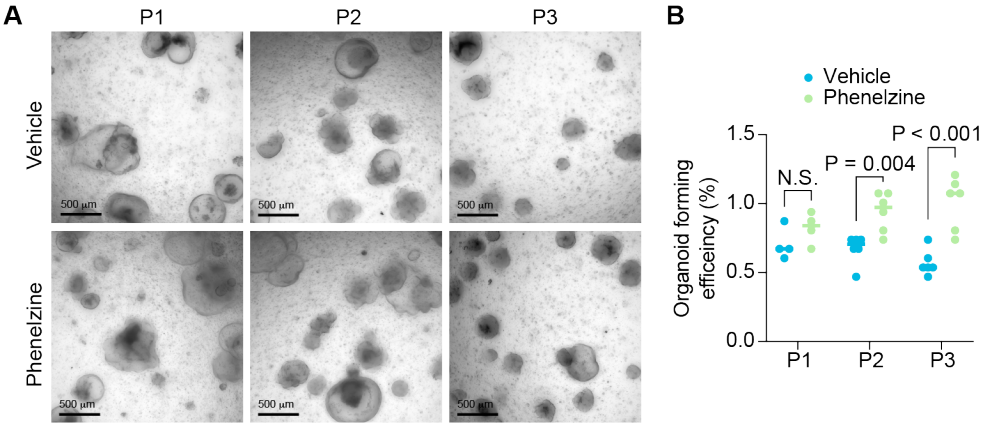

Fig. S14. Phenelzine promotes LO formation.
(**A**) Images of LOs with phenelzine (10 μM) at 12 days of indicated passage. (**B**) Quantification graph of lung OFE at 12 days of passage. Two-tailed Student's *t*-test; error bars: SD. The representative images are shown (n>=3).